Draft version June 25, 2025
Typeset using LaTeX **twocolumn** style in AASTeX7

Discovery of Volatile Gas in the Giant Impact Disk around the 150-Myr old HD 23514

Kate Y. L. Su,[1,2] Attila Moór,[3] Chengyan Xie,[4] Ilaria Pascucci,[4] George H. Rieke,[2] Ágnes Kóspál,[3,5,6]
Mark C. Wyatt,[7] Péter Ábrahám,[3,5,8] Luca Matrà,[9] Zoe Roumeliotis,[9] and D. J. Wilner[10]

[1] *Space Science Institute, 4750 Walnut Street, Suite 205, Boulder, CO 80301, USA*
[2] *Steward Observatory, University of Arizona, 933 N Cherry Avenue, Tucson, AZ 85721–0065, USA*
[3] *Konkoly Observatory, HUN-REN Research Centre for Astronomy and Earth Sciences, MTA Centre of Excellence, Konkoly-Thege Miklós út 15-17, 1121 Budapest, Hungary*
[4] *Lunar and Planetary Laboratory, The University of Arizona, Tucson, AZ 85721, USA*
[5] *Institute of Physics and Astronomy, ELTE Eötvös Loránd University, Pázmány Péter sétány 1/A, 1117 Budapest, Hungary*
[6] *Max-Planck-Insitut für Astronomie, Königstuhl 17, 69117 Heidelberg, Germany*
[7] *Institute of Astronomy, University of Cambridge, Madingley Road, Cambridge CB3 0HA, UK*
[8] *Institute for Astronomy, University of Vienna,Türkenschanzstrasse 17, A-1180 Vienna, Austria*
[9] *School of Physics, Trinity College Dublin, the University of Dublin, College Green, Dublin 2, Ireland*
[10] *Center for Astrophysics, Harvard & Smithsonian, 60 Garden Street, Cambridge, MA 02138, USA*

(Accepted for publication in ApJL)

ABSTRACT

We report the discovery of CO_2 gas emission around HD 23514, an F5V star in the ∼150 Myr-old Pleiades cluster, hosting one of the rare giant-impact disks with unique mineralogy dominated by silica dust. We show that the dust feature remains stable over several decades, and that the sub-μm grains, which give rise to the ∼9 μm feature, are co-spatial with the hot CO_2 molecules within the sub-au vicinity of the star. Examining the Spitzer spectrum taken 15 years earlier, we show that the CO_2 emission was also present at 4.3 σ significance. The existence of tiny silica grains and volatile gas requires special conditions to prevent the rapid loss caused by stellar radiation pressure and photodissociation. We explore several pathways explaining the observed properties and suggest that a past giant impact and/or stripping atmospheric event, involving large bodies with volatile content similar to the carbonaceous chondritic material, can simultaneously explain both the silica and volatile emission. Our discovery provides an important context for the amount of volatiles that a newly formed planet or the largest planetesimals could retain during the giant impact phase in the early solar system evolution.

Keywords: Circumstellar matter (241) — Debris disks (363) — Circumstellar dust (236) — Circumstellar gas (238) — Circumstellar grains (239) — Circumstellar disks (235) — Planetesimals (1259))

1. INTRODUCTION

Young, extremely dusty disks, termed extreme debris disks (EDDs), give new insights into the collisional processes among planetary embryos during the era of terrestrial planet formation. These systems exhibit unique dust mineralogy dominated by thermodynamically altered minerals, likely produced by hypervelocity impacts, analogous to the Giant Impact Hypothesis for the formation of the Moon. The large amount of warm and highly processed dust definitively tie them to the rapid evolution of dust debris in their terrestrial zones, an environment traditionally thought to be dry and devoid of volatiles. Mid-infrared (mid-IR) monitoring shows that the majority of EDDs exhibit significant variability (Meng et al. 2014; Moór et al. 2021; Rieke et al. 2021; Su et al. 2023). In the best studied case of ID8 in NGC 2547, both yearly and monthly semi-periodic variability were observed, which was attributed to the collisional and dynamical evolution of a cloud of escaping boulders and vapor condensates formed in giant impact events (Meng et al. 2012; Su et al. 2019). Deep optical transits

Email: ksu@spacescience.org

have also been found in some highly inclined systems where eclipsing dust clumps are found to be as large as the stars (de Wit et al. 2013; Gaidos et al. 2019; Melis et al. 2021; Su et al. 2022), further validating the scale of such collisions.

HD 23514 (Cl* Melotte 22 HII 1132), an F5V star at a distance of 138.4±0.4 pc (Gaia Collaboration et al. 2021) in the Pleiades cluster, was first discovered to possess an exceptional amount of warm dust and unique dust mineralogy by Rhee et al. (2008). The age of the Pleiades, estimated to be ∼110–150 Myr (Lodieu et al. 2019), makes the system particularly interesting because it corresponds to the final building stage of terrestrial planet formation. After that stage, the rate of colossal Moon-forming events is expected to be significantly reduced (Quintana et al. 2016), consistent with that only ∼1% of the stars younger than a few hundred Myr show detectable 12 μm infrared excesses above 15% levels (Kennedy & Wyatt 2013). To put HD 23514 in perspective, for 100 stars younger than the terrestrial planet formation stage, only one system is like HD 23514. Prior to the end of Spitzer cryogenic mission, Meng et al. (2012) showed that it is also one of the few systems exhibiting IR variability on timescales of a few years. The system shows no sign of cold ($T \lesssim 40$ K) dust and gas, suggesting the disk is compact, likely confined within $\lesssim$10 au (Vican et al. 2016; Sullivan et al. 2022). HD 23514 also has a wide ∼M7 companion at a projected separation of ∼360 au and a position angle of ∼228° (Rodriguez et al. 2012), one of the characteristics that some EDDs share (Zuckerman 2015; Moór et al. 2021, 2024).

The HD 23514 system is one of the only three EDDs where the Spitzer/IRS spectra show prominent silica dust (Rhee et al. 2008; Lisse et al. 2009; Fujiwara et al. 2012), similar to those of the impact glasses and melted droplets commonly found in terrestrial impact craters (Morlok et al. 2016), therefore, they are also called giant impact disks. In the Giant Impact Hypothesis (Canup 2004), the almost fully-grown Earth collided with a Mars-size planet called "Theia" at the end of its formation, and the material from the outer layers of both objects coalesced into the Moon. We can take this well-studied event as a prototype for such impacts. Because the Earth and Moon are almost chemically indistinguishable, Theia was thought to form at a similar distance from the Sun, i.e., dry material with significantly depleted volatile elements – those that vaporize easily upon heating. Some very young debris disks do contain gas, e.g., β Pictoris (Roberge et al. 2000; Dent et al. 2014), but only typically at very young stages ($\leq$ 50 Myr, Moór et al. 2017; Bonsor et al. 2023). Using JWST, we report the truly remarkable detection of hot molecular gas emission in HD 23514, particularly the CO_2 lines have never been detected in debris disks before.

Our observations and basic data reduction are described in Section 2. In Section 3, we describe the findings in terms of (1) lack of large-scale overall excess over four decades and the dust properties showing stable silica emission compared to the Spitzer data taken 15 years earlier, and (2) the properties of volatiles (robust detection of CO_2 and CO, but tentative detections of H_2O and NH_3) and their likely existence in the Spitzer IRS data. In Section 4, we show that (1) the silica dust and gas volatiles are likely co-located within the sub-au region where their lifetimes are less than a year due to radiation pressure blowout and photodissociation, and (2) speculate on the origins of the stable silica dust and that of gas, in which both can be simultaneously explained by invoking a past giant impact event. The conclusion and future prospect are given in Section 5.

2. OBSERVATIONS AND DATA REDUCTIONS

HD 23514 was observed with MIRI/MRS on 2023 Sep 23, as part of the JWST GTO program PID1206 (PI: G. Rieke) to study the dust mineralogy and variability for a handful of EDDs discovered by Spitzer. All MRS channels and subbands were included, covering a wavelength range from 4.9 to 27.9 μm. Each subband was integrated with 12 groups in a single exposure using the FASTR1 mode with a total integration time of 132 s. A nominal observation setup was used, which includes the target acquisition with a neutral density filter, and a four-point dither pattern optimized for point sources.

We used the JWST Calibration Pipeline version 1.15 (Bushouse et al. 2024) and Calibration Reference Data System context `pmap_1298` to reduce the data with default parameter setting and with additional steps for bad pixel self-calibration in the `calwebb_spec2` and residual fringe correction in the `calwebb_spec3` steps[11]. The 12 spectral cubes were inspected visually to identify potential other sources within the IFU field of view. Only a very faint (by a few hundred times) object, ∼2.″3 away from HD 23514 at a position angle of ∼148°, was found in the medium combined IFU images for the data shortward of 18 μm. This faint source is unlikely to be the late-M-type companion reported by Rodriguez et al. (2012) because of very different position angle and projected distance. Given its faintness, it has no impact in the extracted 1-D spectrum. We also examined

---

[11] see MIRI/MRS Pipeline Notebook https://github.com/spacetelescope/jwst-pipeline-notebooks/blob/main/notebooks/MIRI/MRS/JWPipeNB-MIRI-MRS.ipynb

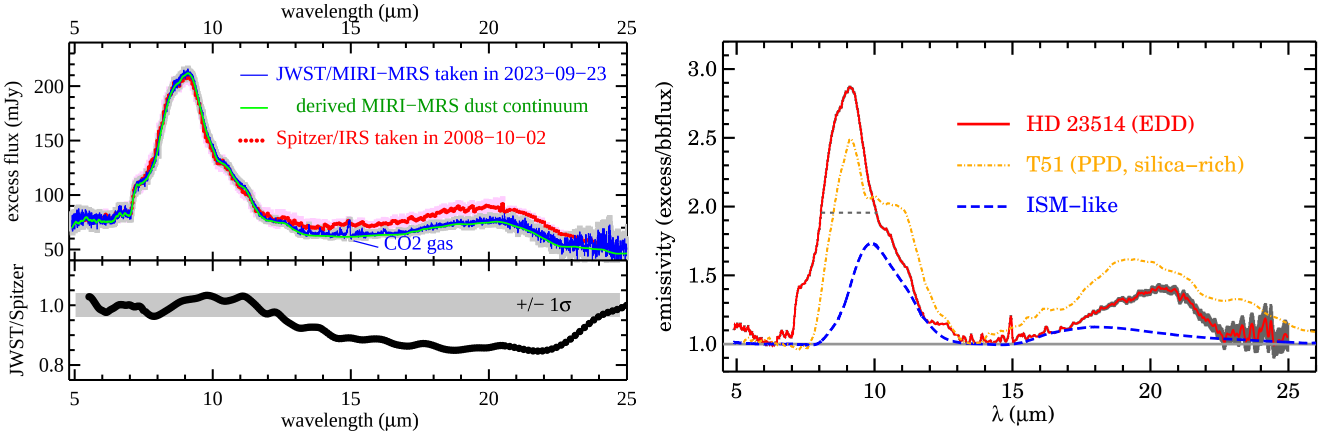

Figure 1. The left panel shows the comparison between the JWST MIRI/MRS and Spitzer/IRS disk spectrum around HD 23514 taken 15 years apart with the bottom one showing the flux ratio between the two. The color shaded area indicates the associated $\pm 1\sigma$ uncertainty. The two spectra agree within $\pm 1\sigma$ in the silica 9 μm region while in the 20 μm region JWST data appear to be slightly lower by $\sim$3 σ. The thin green line is the estimated dust continuum of the JWST data (details see Section 3.3). The right panel depicts the derived dust emissivity spectrum in comparison with a silica-rich protoplanetary disk (orange, dot-dashed line), and a typical ISM-like, very-low-crystallinity dust mineralogy (blue dashed line) (see Appendix A for details).

the target spatial extension by comparing with a calibration star at all observed wavelengths, and concluded that the HD 23514 system is point-like and not resolved by JWST.

A 1D spectrum was extracted for each of the cubes using the default aperture and sky annulus (Law et al. 2025) that increased linearly with wavelength. Finally, to improve the continuity of the full spectrum, a small flux shift ($\lesssim$a few %) was applied to individual spectra using the overlapping wavelength region and lining up with the shortest subband. Because the star contributes significant flux in the short wavelength part of the MIRI/MRS spectrum, we derive the disk emission by subtracting a model photosphere (details see Appendix A), yielding the spectrum shown in Figure 1 (left).

3. RESULTS AND ANALYSIS

3.1. *Lack of large-scale variation*

As shown in Figure 1, the disk emission (in both flux level and solid-state feature) is remarkably similar to the one taken by Spitzer/IRS 15 years earlier. The prominent 9 μm silica feature agrees very well within $\pm$5% (1 σ uncertainty including the absolute flux calibration from both observatories), while in the broad 20 μm feature region the JWST data are consistently lower by $\sim$15% compared to the Spitzer one at $\sim$3 σ significance. This behavior suggests that there is no significant change in terms of dust composition, but the dust temperature is slightly lower in the JWST epoch (by $\sim$20 K, see Appendix A). The HD 23514 disk is known to display both weekly and yearly, stochastic IR variability, at $\sim$10–30% level in both the 3–5 μm and 24 μm photometry (Appendix B). Because there are no dust features in those bands, the variability is likely due to the change in the dust temperature rather than the composition. The overall level of the 10 μm feature has not changed appreciably over a 40-year baseline from the earliest IRAS 12 μm measurement taken in 1983, AKARI 9 μm taken in 2006, WISE 12 μm measurement taken in 2010 to the latest JWST data taken in 2023 (details see Figure B2). Lack of large-scale variation in the 10 μm feature over decades has also been reported for other EDDs like HD 113766 and HD 172555 (Su et al. 2020; Lisse et al. 2009; Samland et al. 2025).

3.2. *Dust Properties*

To characterize solid-state features, we derived the dust emissivity (observed spectrum divided by the featureless dust continuum) and estimated the crystalline mass fraction indices following the method outlined by Watson et al. (2009) for protoplanetary disks (PPDs). Because debris disk structures generally are not as complex as the PPDs, we use a combination of two blackbody functions to estimate the featureless dust continuum (Appendix A.2). The derived emissivity (smoothed to a resolution of $R = 500$ for clarity) is shown in Figure 1 (right).

The mineral features are key in dust composition identifications due to stretching and bending motions in the silicon-oxygen anions. The narrow and strong resonance features from the thermally processed, crystalline silicates are easily distinguishable from the broad features of amorphous grains lacking ordered structure (Henning 2010). The mass fraction of crystalline grains present in an infrared spectrum is then a good indication for the thermal processing in the disk environment (Sar-

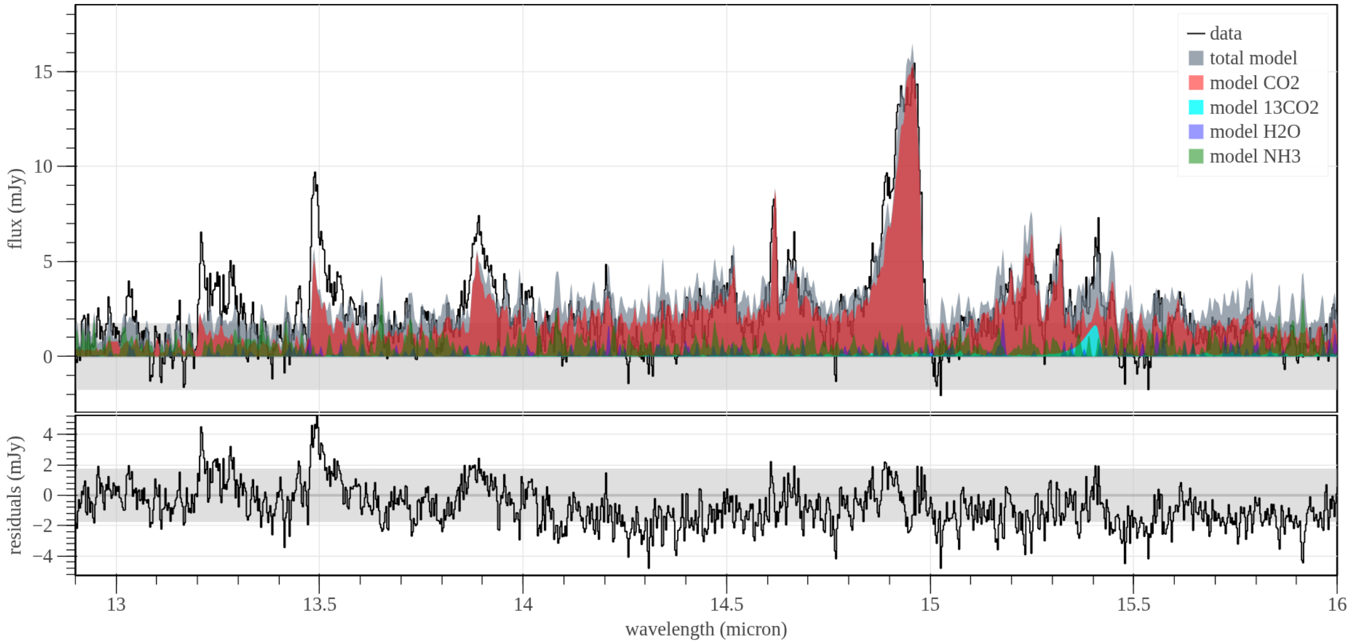

Figure 2. Zoom-in, continuum subtracted spectrum centered at ∼15 μm showing the dominant CO_2 Q-, P-, and R-branch molecular lines in the upper panel and the residuals (data − model) in the bottom panel. The black line depicts the data with the gray horizontal area showing the ±1 σ estimated in the local spectral region. Filled, color areas show the model emission from four volatile species: CO_2, H_2O, NH_3 and $^{13}CO_2$ with the dark gray area showing the model sum.

gent et al. 2006; Juhász et al. 2010). Watson et al. (2009) defined three crystalline mass fraction indices for the strongest features of pyroxenes (P_{10}), olivines (O_{10}) and silica (S_{10}) in the 10 μm complex, centered at wavelengths 9.21, 11.08, and 12.46 μm, respectively, by referencing to a pristine (ISM-like, amorphous) silicate feature (for details, see Watson et al. 2009). An index value is roughly unity when the emission feature resembles the pristine profile, while an index value above unity reflects increasing prominence of a crystalline signature above the pristine one. The three indices are simple proxies for the amount of crystalline (thermally processed) grains without detailed dust decomposition modeling. Because the ∼9 μm silica peak can overlap with the 9.21 μm pyroxene peak under low spectral resolution, the silica index is defined by the narrow feature at 12.5 μm. In other words, the prominent 9 μm silica feature seen in HD 23514 is not entirely captured by the silica index (S_{10}). Although these indices do not perfectly track the exact level of crystallinity on individual bases, they are good indicators when comparing properties among an ensemble of objects (Watson et al. 2009).

Using the derived dust emissivity, the 10 μm emission complex in HD 23514 can be described as having a peak wavelength at 9.1 μm with a full-width-half-maximum (FWHM) of 2.04 μm, an equivalent width (W_{10}) of 4.7±0.2 μm, P_{10}=2.54, O_{10}=0.91, and S_{10}=1.82. These crystalline indices suggest that the crystalline dust in HD 23514 is dominated by both pyroxene and silica with little of olivine type. The crystalline mass fraction is high (∼40% using the pyroxene index with the empirical trend derived by Watson et al. 2009), which is not common among PPDs. Silica dust has been found in a handful of PPDs, and one example (around a few Myr PPD, T51 (Sz 41)) is also shown in Figure 1 (right) for comparison. The 10 μm dust emissivity comparison between HD 23514 and the young star (Appendix A.2) suggests that the dust in HD 23514 has a higher crystallinity and the dominant dust size is smaller than that of the PPD (∼μm) as evidence by the feature's FWHM. Furthermore, the W_{10} (an indication for the amount of small grains) of 4.7 is also near the top among the 84 PPDs observed by Spitzer (only three systems have W_{10} over 5 and all have near unity crystalline indices, i.e., low crystallinity fraction). The highly thermally processed dust mineralogy implies different formation processes. As detailed in Section 3.1 and Appendix A.2, past giant impact events are the most likely mechanism responsible for the large amount of highly processed crystalline silicates and silica grains in HD 23514.

3.3. *Surprising Molecular Gas Emission Lines*

In addition to the prominent silica feature, the high quality JWST spectrum also reveals surprising gas emission lines. Visual inspection indicates that the lines are dominated by CO_2 emission centered at 14.98 μm (Q branch) accompanied by the P and R branches on the short- and long-wavelength sides. To properly characterize the molecular lines and discover other weaker ones, the dust continuum emission needs to be removed from the spectrum. The continuum was determined in an iterative way as detailed in Appendix C.1 and shown in the left panel of Figure 1. A subset of the continuum subtracted spectrum centered at ∼15 μm is shown in Figure 2 while the rest is shown in Figures C6 and C7.

We used the local standard deviation per channel and subband as the typical root mean square (rms) of the continuum-subtracted MRS spectrum after masking out strong detected lines. Although the overall signal-to-noise ratio (S/N) of the data before continuum subtraction is >100 for λ <20 μm, unresolved emission lines with fluxes $\lesssim$5 mJy cannot be robustly detected in the current data. Despite the hints of H_2O, and NH_3 present in the spectrum, only CO_2 Q-branch is detected at 10 σ along with the R and P branches at 3–5 σ, and CO at 2–4 σ. There is no sign of molecular/atomic hydrogen and hydrocarbon lines that are commonly found in PPDs, nor ionized/neutral atomic lines such as [Ne II], [Ar II], [Fe II], [Ni II], [Cl I], and [S I] present in HD 23514. Non-detection of molecular/atomic hydrogen and [Ne II] lines is the best indication that the gas in HD 23514 is not primordial but secondary (Pascucci et al. 2007), which is also consistent with the estimated upper limit for the CO-to-H_2 mass ratio (Appendix C.2).

To extract basic properties of the emitting gas, a plane-parallel slab model in local thermodynamic equilibrium (LTE) was adopted using three parameters: the gas emitting area (A), column density (N), and the gas temperature ($T_{\rm gas}$). The emitting area is often expressed as an equivalent emitting radius ($R_{\rm em}$) where $A = \pi R_{\rm em}^2$. We focused on fitting the CO_2 complex in the 13.5–16.3 μm region where the detected lines have the highest S/N. Assuming a turbulence velocity of zero, we find that a slab model with A =0.0085 au^2 (or $R_{\rm em}$ =0.052 au), N =1.38×10^{18}cm^{-2}, and $T_{\rm gas}$ =891 K can reproduce the CO_2 emission spectrum well. The associated uncertainties could be large (for details, see Appendix C.1), mostly due to the LTE assumption where the inferred temperature is higher, which could lead to an order magnitude lower column density than that in non-LTE (Bosman et al. 2017).

Due to low S/N in most of the continuum-subtracted spectral region, we simply adopted similar parameters for H_2O, NH_3 and adjusted them to achieve reasonable fits visually. For CO, the same approach produces much narrower line widths in the limited wavelength range covered by MIRI/MRS, while an extra broadening along with a hotter gas temperature model can also reproduce the data (for details see Appendix C). Overall, the simple slab models can roughly match the peak flux of the CO lines in both cases, but the hotter one matches the line profiles better. We consider the detection of volatile CO_2 and CO is robust, and the H_2O and NH_3 detections are tentative. Using the LTE slab model, the properties of CO_2 are well constrained, but less so for CO and not at all for H_2O and NH_3. Non-LTE effects are particularly important for the low-density region that is very close to the star. Exploring non-LTE models is beyond the scope of the paper, which needs high S/N data (particularly for many of the weak water lines) and shorter wavelength coverage between 4.4 and 4.9 μm where the CO lines are brighter. Using LTE models we show that the JWST MIRI spectrum indubitably reveals the presence of hot (∼900 K) gas in the sub-au (∼0.03–0.05 au) region around HD 23514.

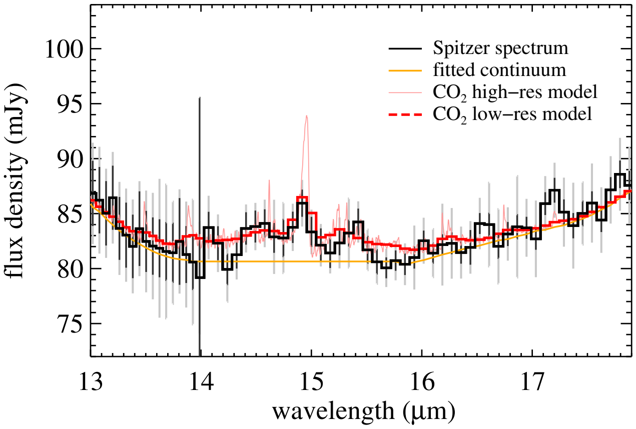

Figure 3. Spitzer IRS low-resolution spectrum of HD 23514 observed in 2008 centered at the CO_2 15 μm complex where the data is shown as the black line with 1σ rms error showing as dark vertical lines (gray for the combined error). The thick red line is the expected, low-resolution model spectrum if the same level of the CO_2 emission detected by JWST (thin red line) was also present. This comparison suggests that the same CO_2 emission is presented in the Spitzer spectrum where the brightest Q-branch line is detected at 4.3 σ.

3.4. *Is CO_2 present in the Spitzer/IRS spectrum?*

Inspired by the discovery of CO_2 gas, we went back to examine whether a similar gas emission was also present in the Spitzer IRS spectrum taken 15 years earlier. We retrieved the calibrated spectrum from the Combined Atlas of Sources with Spitzer IRS spectra (CASSIS)[12] (Lebouteiller et al. 2011) site. We used the optimal extraction product best for point sources and adopted the uncertainty including both statistical (rms) and system-

---

[12] https://cassis.sirtf.com/atlas/

atic errors. The IRS data shown in Figure 3 do show a bump near 15 μm, which was not found in other similar debris systems (for details see Appendix C.4), suggesting that the bump is likely astrophysical in nature. We then determined the general continuum by fitting the CO_2 complex region using a polynomial function and forcing the flux between 13.9 and 15.8 μm to be relatively flat for a conservative approach as shown in Figure 3. We then constructed a low-resolution model spectrum by (1) adding the JWST CO_2 model (from Section 3.3) to the continuum, and (2) re-sampling the wavelength grid to match the Spitzer IRS spectral resolution[13]. As shown in Figure 3, the low-resolution model spectrum resembles the observed one well if the same level of the CO_2 emission detected by JWST was also present. In this case, the strong CO_2 Q-branch was detected at 4.3 σ statistically (2.5σ if using the combined error) while the others were buried in the noise. In summary, the same level of the hot CO_2 emission is also present in the Spitzer data taken 15 years earlier and remains unchanged between the two epochs.

4. DISCUSSION

4.1. *Colocation of silica and hot gas*

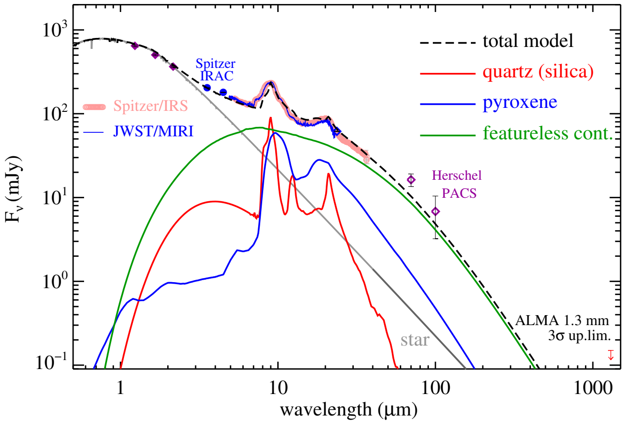

Figure 4. The SED of the HD 23514 system where the data points come from 2MASS, Spitzer and Herschel photometry along with the mid-IR spectra. Lines show the SED models for a disk in a radial range of 0.1–3 au and a dust composition mixture of silica and pyroxene, and grains lack of insipid features. The prominent 10 and 20 μm features mostly come from optically thin silica and pyroxene grains within sub-au (for details, see Section 4.1 and Appendix D).

The HD 23514 system has been observed with the near-IR adaptive optics imaging at the 10 m Keck II telescope (Rodriguez et al. 2012) and with ALMA at 1.3 mm using a beam size of $1\overset{''}{.}5$ (Sullivan et al. 2022), and neither resolves nor detects the disk. Despite the high degeneracy, the disk extent can be estimated using spectral energy distribution (SED) models because the bulk of disk emission is sensitive to its temperature (i.e., location for a given dust composition). Vican et al. (2016) characterized the HD 23514 system as a two-temperature disk with a hot component having dust temperatures ($T_{\rm d}$) of ∼1082 K and a warm component with $T_{\rm d}$ of ∼168 K, roughly consistent with our estimated temperatures for the featureless dust continuum (750 + 200 K; Appendix A). Given the stellar properties, these temperatures correspond to radial locations of ∼0.1 and ∼4.8 au, respectively, for blackbody emitters. For imperfect emitters like dust grains, the probable location is likely to be larger (Figure C9). Under the optically thin condition, the contrast/ratio between the prominent 10 and 20 μm dust features is a good proxy for dust temperature as that the larger the ratio the hotter the dust is due to the Planck emission (Figure C9). In other words, the bulk of the dust emission that gives rise to the silica feature most likely comes from the hot rather than the warm component.

We explored SED models, aiming to constrain the location of the silica dust (for details see Appendix D). Although such models might be degenerate, they provide diagnostic constraints under simplified assumptions. We found that the minimum grain size in the disk needs to be 0.1–0.5 μm in order to reproduce the 10/20 μm feature strengths, which is smaller than the typical blowout size, ∼1 μm for HD 23514 (Appendix D.2). Our SED models suggest that the disk is compact (∼0.1–3 au), and the highly refractory silica grains are mostly confined within the sub-au region, where the temperature is close to their sublimation temperature, in order to reproduce the prominent 9 μm feature and 3–5 μm flux. The system's infrared fractional luminosity is 1.76×10^{-2} with ∼70% coming from the featureless dust continuum. The total dust mass is $\sim10^{24}$ g ($1.67\times10^{-4} M_\oplus$) and the feature-producing grains account for ∼5% of the dust mass with only ∼1% coming from tiny silica dust. Based on the model parameters for the gas (Section C.1) and the silica dust, they are likely co-located very close to the star at sub-au distance.

4.2. *Origins of the Stable Silica Dust*

The origin of the large amount of sub-μm grains in debris disks has been long debated in the literature. The typical radiation pressure blowout size is ∼1 μm around HD 23514 except for highly porous grains (Arnold et al. 2019), i.e., the grains that give rise to the prominent mid-IR feature have very short lifetimes (less than a

---

[13] see the IRS Instrument Handbook for details

year, Appendix D.3). This implies a very high mass loss rate (5×10^{22} g yr^{-1}) if there were no optical depth effects either to prevent them leaving the system by shielding or to replenish them fast enough (e.g., Thebault & Kral 2019). If this high rate was sustained through collisional cascades over the age of the system (150 Myr), HD 23514 would need to be born with a disk that is 35 times of the minimum mass of solar nebula (MMSN), which is not impossible but unlikely. Instead, the large amount of small grains is more likely to be created by transient events where the high rate is only applicable for a limited recent time. The maximum dust production rates in solar system comets can reach $\sim10^{13}$ g yr^{-1} when they are very close to the Sun. It is then unlikely to sustain the high dust production/loss rate by inward scattered comets if these grains are continuously being ejected by radiation pressure.

One easy way to address this dilemma is that all or some portion of the small grains are not subject to radiation pressure blowout, which can be achieved by certain grain properties or being trapped by other means (Rieke et al. 2016; Lebreton et al. 2013; Pearce et al. 2020). The prominent $\sim$9 μm feature is thought to come from obsidian or annealed/fused quartz grains (Fujiwara et al. 2012) whose properties make them transparent to stellar photons, therefore not subject to blowout, when they are tiny enough (Artymowicz 1988). Giant impacts provide perfect conditions for the tiny grain formation. These tiny grains could have been generated either by direct condensation from the impact-produced vapor (Johnson & Melosh 2012) or by hyper-velocity grinding within optically thick clouds of debris produced by violent collisions of large bodies (Johnson et al. 2012). In the former case, these silica grains were born tiny; while in the later case, tiny grains were formed through collisional cascades and the optical depth effects within the formation region allow grains that are much smaller than the blowout size to form. As a result, the solid-state feature rising from the tiny silica dust would remain stable until they slowly drift inward due to the Poynting-Robertson drag (Su et al. 2020). The feature would gradually weaken due to dust sublimation once the grains reach the sublimation temperature under timescales of a few hundred years in HD 23514.

In addition, the giant impact ejecta would also form a population of planetesimals, maintaining a high level of dustiness and creating temporal variation (Watt et al. 2024) as probed by 3-5 μm photometry. The observed variability levels require a minimal corresponding area change in the dust cross section to be on the order of (1–2.5)$\times10^{-3}$ au^2 (for details see Appendix B). This dust cross section is similar to the emitting area of hot gas, pointing a potential link between the dust and molecular gas production in the sub-au region. Assuming the molecular gas and small dust share the same sub-au region, the estimated gas and dust masses suggest that the small grains could have low (<1) Stokes number and coupled with the gas (highly depending on the estimated CO mass, see Appendix C.1). The presence of molecular gas would increase the dust-clearing timescale due to the combination of radiation pressure and gas drag (Takeuchi & Artymowicz 2001; Kenyon et al. 2016). Exploring grain trapping is beyond the scope of this paper, but it is likely to be an important component to a comprehensive model for the HD 23514 system, particularly in light of the new discovery of gas in the system.

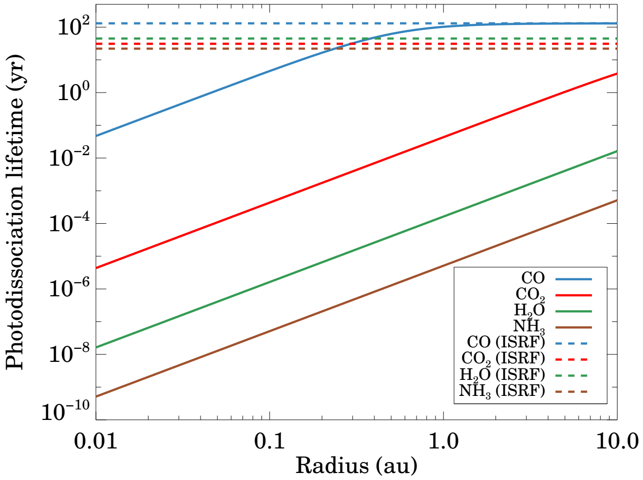

Figure 5. The photodissociation lifetime of unshielded molecules as exposed to both the ultraviolet (UV) photons from HD 23514 and the interstellar radiation field (ISRF) as a function of stellocentric distance where the dashed lines are those only using ISRF. The UV emission from the star was estimated using the Kurucz model (Appendix A.1), which under estimates the amount of UV photons given its youth. The unshielded photodissociation lifetimes shown here should be considered as upper limits.

4.3. *Origins of the Volatile Material*

Under the optically thin condition, molecules have very short photodissociation lifetimes, particularly around an F-type star like HD 23514. Figure 5 shows the expected unshielded photodissociation timescales for various molecules as a function of stellocentric distance from the star. Volatiles would only survive much less than a year once released within 1 au including additional shielding as detailed in Appendix C.3, but CO could persist over $\sim$100 years outside 1 au. The detection of hot molecular gas suggests that these molecules require a continuous replenishment and/or an effective protection/shielding against the strong stellar radiation.

The short-lived volatiles in the very close (<1 au) vicinity of the star can be produced either in-situ or delivered from the outside 1 au region as discussed below.

In-situ Formation In the context of the giant impact hypothesis, molecular gas could be produced by outgassing processes if one or both the impacting bodies are volatile-rich. Earth's early atmosphere was thought to form by retention of these outgassing products (Abe & Matsui 1985). Impact experiments and model calculations both show that H_2O and CO_2 are the major gases produced by outgassing of carbonaceous chondritic material over a wide range of temperatures and pressures (e.g., Lange & Ahrens 1982; Schaefer & Fegley 2010; Thompson et al. 2021, and references within). Furthermore, shock-recovery experiments targeting a mixture of olivine, iron and water also reveal preferential formation of ultrafine (tens of nanometers) smoke particles of silicates and metal oxides, facilitated by the role of supercritical water (Furukawa et al. 2007). These tiny grains might be ubiquitous in post ocean impact events and provide effective UV shielding for the volatiles. Alternatively, the volatiles could also be released from (1) an atmospheric stripping event as has been suggested for HD 172555 (Schneiderman et al. 2021), or (2) the large remnants of a giant impact ejecta as long as they are large enough to retain a significant fraction of volatiles. It is then interesting to note that the change in the dust cross section (derived in Appendix B) is on the same order as the emitting area of the molecular gas, indicating that collisional activities in the aftermath of giant impact events could be tied to the formation/protection of molecular gas in the inner region.

Delivery from Outer Region This delivery scenario has been widely accepted in both our solar system (comets) and other debris systems (exocomets) – scattered icy bodies from the outer region releasing volatiles and dust grains as they warm up on their inward migration. In this case, the detected molecular gas might have no direct relationship with the giant-impact-produced small grains observed in the system. For HD 23514, the inward delivery rate might be much lower than that of the debris systems that host Kuiper-belt analogs such as β Pic (Beust et al. 1996; Matrà et al. 2019) and η Corvi (Marino et al. 2017) because it has a limited volume of cold reservoir for storing icy bodies (lack of a massive Kuiper-belt analog, see Appendix D). This scenario also needs a perturber either internally or externally to efficiently scatter icy bodies into the inner region. Ground-based high contrast imaging found no other sources within 10″ around HD 23514 except for the M7 brown dwarf companion (Rodriguez et al. 2012) 2.″64 away, while a recent RV study rules out massive giant planets within 0.1 au (Takarada et al. 2020). External companions under some favorable conditions can excite the planetesimal population via the eccentric Kozai–Lidov mechanism, leading to inner dust and gas production (Naoz 2016; Young & Wyatt 2024). Without detailed orbital parameters, it is not clear whether the M-dwarf companion at ∼360 au away is capable of this role. Other challenges in the delivery scenario are: (1) evaporation of icy bodies is expected to occur at a range of distances, which is at odds with the gas concentration within the sub-au region, and (2) the comet delivery rate is expected to be variable based on the solar system observations, which somehow contradicts the tentative CO_2 detection in the Spitzer data. The second challenge might be accommodated if scattering of many comets at a high efficiency. A future investigation is needed to further explore the delivery model; nonetheless, it remains a possible origin for the molecular gas.

5. CONCLUSION

We have presented a JWST MIRI/MRS 5–28 μm spectrum of HD 23514, an F5V star in the ∼150 Myr-old Pleiades cluster, hosting one of the giant-impact disks discovered by Spitzer with unique mineralogy dominated by ∼9 μm silica dust. We found that the prominent silica feature remains stable compared to the data taken 15 years earlier by Spitzer, and that the system lacks large-scale (>30%) variation over a 40-year baseline since the IRAS measurement taken in 1983. Characteristics derived from the observed dust mineralogy and SED modeling suggest that the dust has high crystalline mass fraction preferentially in both pyroxene and silica types with the latter mostly confined within sub-au region. The JWST spectrum also reveals surprising hot molecular gas emission from CO_2 and CO with traces of other volatiles such as H_2O and NH_3, apparently stable as seen in the Spitzer data and co-located with the silica dust. We explored several pathways explaining the observed properties of dust and gas, and found that a past giant impact event can simultaneously explain both the large amount of highly processed small grains (crystalline silicates and silica) and volatile emission.

In the preferred giant impact scenario, at least one of the involved bodies needs to have volatile content similar to the carbonaceous chondritic material in the solar system. Volatiles are expected to form as (1) the outgassing products either directly from the newly formed, molten planet or from the large planetesimal remnants of impact ejecta, or (2) the stripped atmospheric material. Tiny silica grains can form either by direct condensation from the impact-produced vapor or by hyper-velocity grinding within pebble-size, vapor condensates. If one of the impacting bodies had a surface ocean before the violent collision, the post ocean impact event also favors the formation of ultrafine particles, which can also provide effective UV shielding for the volatiles.

Alternatively, the tiny silica and molecular gas have no direct relation and are created by non-related processes. Volatiles can be delivered into the inner planetary region from scattered icy bodies originally stored in the outer reservoir. Erosion of a rocky body in a high temperature environment can produce tiny silica dust by degradation of silicates. The keys for these alternatives are whether these processes can be efficient enough to account for the amount of silica and molecular gas observed in the system. Future observations to better determine the gas properties, search for other warm/cold gas and dust, assess the temporal change in both the dust composition and volatiles, and identify the shielding mechanisms against photodissociation will help to shed more light into the EDD phenomenon.

APPENDIX

A. STELLAR PROPERTIES AND DUST EMISSIVITY CALCULATION

A.1. *Stellar Photosphere and Subtraction*

For the stellar emission, we used a Kurucz model of T_*=6500 K and logg=4.5, normalized to the optical and JHKs photometry corrected by an interstellar extinction of A_V=0.1 (Román-Zúñiga et al. 2023). Given a distance of 139 pc, the integrated stellar luminosity is ∼3 $L_\odot$ and the stellar radius is 1.4 $R_\odot$. These values are all consistent with the values found in the literature for a 1.3 $M_\odot$ young star (Rodriguez et al. 2012; Fu et al. 2022; Román-Zúñiga et al. 2023). This stellar model was used for deriving IR excess, computing thermal equilibrium dust temperatures in SED modeling, and photodissociation rate of molecules.

The stellar emission contributes to the majority of the emission shortward of 2.2 μm. Using the Kurucz model, we determine the star has a integrated flux of 153 and 99 mJy for the Spitzer/IRAC I1 and I2 bands, respectively, but 170 and 95 mJy for WISE W1 and W2 bands (due to the different filter profiles). HD 23514 has been monitored by the Kepler and TESS missions. Gaia DR3 catalog gives $T_{\rm eff}$, logg, [Fe/H], RV as 6319 K, 4.21, -0.24 and 6.32±0.44 $\rm km\,s^{-1}$. Tsantaki et al. (2022) lists its RV as 5.18±0.28 $\rm km\,s^{-1}$ and Mermilliod et al. (2009) lists its V sin$i$ as 49.5±5 $\rm km\,s^{-1}$. The system shows no flaring behavior (Ilin et al. 2019), nor δ Scuti-like pulsations (Bedding et al. 2023) over the monitoring periods. Assuming the star is stable over time, Appendix B discusses the IR variability of the HD 23514 system using archival data from Spitzer and WISE. Figure A1 shows the comparison in the MRS spectrum before and after stellar subtraction, suggesting that the IR excess has a roughly equal contribution as the stellar photosphere at 5 μm (the shortest wavelength of MRS).

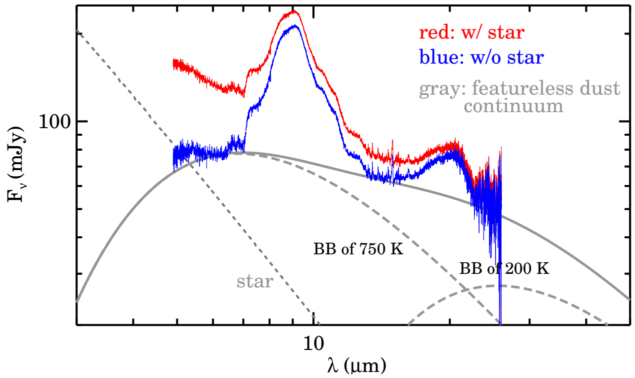

Figure A1. MIRI MRS data before (red) and after (blue) stellar photosphere subtraction. The gray line represents the featureless dust continuum with a combination of two blackbody emission at 750 K and 200 K. This featureless dust continuum was used to compute the dust emissivity as shown in the right panel of Figure 1.

A.2. *Dust Emissivity & Silica Properties*

There are a few ways to determine the featureless dust continuum (termed "pseudocontinuum"). Watson et al. (2009) used a fifth-order polynomial function anchored at the wavelength range where the dust emission feature is small for a large sample of PPDs observed by Spitzer/IRS. Harker et al. (2023) analyzed a large sample of solar system comets observed by Spitzer/IRS, and they used a scaled Planck function as the pseudocontinuum defined as spanning λ =7.3–7.7 and 12.3–13.0 μm to study the 10 μm feature complex. For the JWST/MIRI/MRS spectrum, we decided to use a combination of two Planck functions as the pseudocontinuum by anchoring the wavelength regions that have minimal contribution from known solid-state dust features. As shown in Figure A1, the pseudocontinuum as represented by ∼750 and ∼200 K Planck functions captures the featureless dust continuum well (after stellar subtraction). The resultant dust emissivity is shown in the right panel of Figure 1.

To further validate our approach, we also generated dust emissivity functions for a young star called LkCa 15. The dust emissivity in LkCa 15 was classified as an ISM-like profile by Watson et al. (2009) where the emission is dominated by pristine silicate dust grains (i.e., amorphous and sub-micron). Therefore, we used its mid-IR archival spectra from Spitzer/IRS and JWST/MRS as the input and constructed the pseudocontinuum using the polynomial function for the former but a combination of two blackbodies for the latter. The resultant two dust emissivity functions agree well within a few percent in the 10 μm complex (5–14 μm), but in the 20 μm complex the JWST one is slightly higher by $\sim$20–40% likely due to the limited long-wavelength in determining the pseudocontinuum. The derived JWST LkCa 15 dust emissivity is shown in the right panel of Figure 1. Because our focus is in deriving the crystalline mass fraction indices by referencing the ISM-like profile in the 10 μm complex, the difference in the 20 μm region has no impact on the result. We used the JWST LkCa 15 emissivity function to compute the indices (P_{10} for pyroxene, O_{10} for olivine and S_{10} for silica) as defined by Watson et al. (2009). Note that these indices are defined as the normalized ratio in dust emissivity at a certain wavelength range covering the narrow features, the normalization of the reference (ISM-like) emissivity (i.e., the blue curve in the left panel of Figure 1) has no effects on the results. For HD 23514, the derived indices are: P_{10} =2.54, Q_{10} =0.91, and S_{10} =1.8, suggesting a high fraction of crystallinity preferentially in the pyroxene and silica mineralogy. We also derived the dust emissivity using the Spitzer IRS spectrum, and found similar indices within the uncertainty (corroborating no change in the dust composition).

To quantitatively characterize the silica feature in HD 23514, we also derived the dust emissivity using the Spitzer IRS spectrum of T51 (a few Myr-old star). T51 is one of the five silica-rich PPDs characterized by Sargent et al. (2009) who found that the system lacks sub-μm amorphous dust and the crystalline silicate mass fraction is $\sim$15% including both pyroxene and olivine types, and the silica dust is best scribed as annealed silica although obsidian or amorphous quartz give equally good fits. Our derived indices for T51 are: P_{10} =2.02, Q_{10} =1.50, and S_{10} =2.36, respectively, consistent with the finding in HD 23514 above. Although the 10 μm feature in T51 and HD 23514 both peaks at 9.1 μm (Figure 1 right), the FWHM of the 10 μm feature in T51 is 1.5 times larger, suggesting the dominant size in HD 23514 is smaller, likely sub-μm.

Silica is not abundant in the ISM. Its presence in circumstellar disks requires special conditions for formation like giant impacts as we discuss here. Space weathering, as discussed by Sargent et al. (2009), is one way to deposit silica by converting silicate minerals; however, it is unlikely to be the primary mechanism responsible for the large amount of sub-um size silica seen in HD 23514. Space weathering is a long-term process. $\sim\mu$m-size silicate grains in the inner region of HD 23514 have short lifetimes (blowout size is 1 μm, and will be gone on orbital timescales), implying that converting small silicates, produced by collisional cascades, to silica is an inefficient process. For stars just emerge from the protoplanetary disk stage, massive flare events could speed up the process as suggested by Lisse et al. (2020), however, HD 23514 is not very active at an old age of 150 Myr (Appendix A.1). Comets could bring a large amount of fresh dust into the inner region during a period of high delivery rates like the late heavy bombardment, and create silica through space weathering. For solar system comets, the dust mass is $\sim10^{14}$ g on average (Harker et al. 2023), meaning a total of 10 billion comets is needed to account for the dust observed in HD 23514 ($\sim10^{24}$ g derived in Appendix D). The most challenging problem in the comet delivery scenario is that the typical dust size is large, $\sim$100 μm (Rinaldi et al. 2017), i.e., space weathering should produce large-size silica, not sub-μm. In summary, the proposed giant impact scenario is the most likely explanation for the large amount of sub-μm silica grains in HD 23514.

B. OTHER MID-INFRARED DATA AND 3–5 μm PHOTOMETRIC MONITORING

HD 23514 has various space- and ground-based mid-IR photometry, with the earliest measurement from IRAS in 1983 (Moshir et al. 1992; Ishihara et al. 2010; Rhee et al. 2008; Wright et al. 2010; Meng et al. 2012). Figure B2 summarizes these photometric observations between 5 and 25 μm. The plotted data have been color corrected using the Spitzer/IRS spectrum, assuming that it is a good representation of the SED shape in the given wavelength range over the period of interest (1983–2010). Because WISE 12 μm band was selected to match approximately that of IRAS (Cutri et al. 2012), they trace the same part of the 10 μm feature. The color corrected flux densities in these WISE and IRAS bands are 102.9±4.8 mJy and 131.6±18.4 mJy, respectively, i.e. the two fluxes agree within the 1.5 σ photometric uncertainty.

IR variability within $\sim$20–30% levels, as an additional hallmark commonly found in the extreme debris disks (Moór et al. 2021), is known for HD 23514 (Meng et al. 2012). HD 23514 has been intensively monitoring by Spitzer/IRAC and WISE at 3–5 μm with the former in

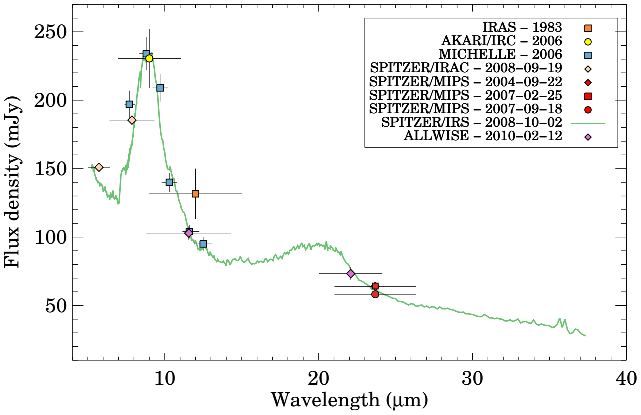

Figure B2. IR photometry of HD 23514 available in the literature/archive before 2013 in comparison with the Spitzer IRS spectrum. The horizontal bars show the bandpass of the measurement while the vertical ones for the 1-σ uncertainty.

∼3–day cadence when available, while the latter in ∼6–month cadence. Following the analysis method used for another IR variable, the RZ Psc disk (Su et al. 2023), Figures B3 and B4 show the short- and long-term disk fluxes at 3–5 μm between 2008 and 2024 where the two epochs of the IR spectra were also marked.

Using these 3–5 μm data, the HD 23514 disk exhibits stochastic, both weekly and yearly IR variability with a weak, positive trend between the excess flux and color temperature. The inferred color temperatures are ∼700–800 K, consistent with the warmer dust temperature inferred from the featureless pseudocontinuum in Appendix A.2. The typical peak-to-peak flux variation (Figure B3) is ∼15% in both the 3.6 and 4.5 μm bands, more than 10 σ significance compared to the photometry stability (∼1%) determined by the field stars in the data. The 14-year long WISE data (Figure B4) show a similar behavior with the largest peak-to-peak flux difference of ∼25 mJy in the W2 band. Taking the typical (∼10 mJy) and maximum (∼25 mJy) 4.5 μm flux change at a face value, the *minimal* corresponding area change in dust cross section is (1–2.5)$\times 10^{-3}$ au^2 by adopting a dust temperature of 800 K and a distance of 139 pc under optically thin assumption. It is interesting to note that this minimal area change in the dust cross section is similar to the hot CO_2 gas emitting area (Table C1). The cross section changes can also be translated to the *minimal* change in the dust mass (assuming static state collisional cascades down to the radiation blowout size of ∼1 μm). The very lower limit on the associated dust mass is on the order of ∼3–7$\times 10^{21}$ g, corresponding to the total disruption of a >120–165 km-size asteroid (assuming a density of 3.5 g cm^{-3}). This mass/size is a lower limit because of our assumptions (optically thin and static state).

C. GAS MODEL AND OTHER RELATED CALCULATION

C.1. *LTE Slab Model*

For the LTE slab gas modeling, we first need to determine the gas contribution to the total emission by determining the dust emission, which includes both solid-state and featureless continuum. To fit the continuum of the spectrum, we applied a median smoothing and a second-order Savitzky–Golay filter, and used the procedure presented in Pontoppidan et al. (2024) to apply a final offset based on line-free regions. We excluded the bad negative pixels in the continuum fitting using `scipy.signal.find_peaks` with a prominence of 0.008. Because the visual inspection showed that CO_2 is the most dominant feature in the data, we also excluded the wavelength range around the CO_2 emission (14.78 μm< λ <15.0 μm) and the tentative NH_3 emission (10.32 μm< λ <10.7 μm). This assumption excludes the potential pseudo-continuum produced by optically thick molecular emission (visual inspection does not find such a emission), a limitation of modeling gas and dust separately (Liu et al. 2019). The resulting continuum fit is shown in the left panel of Figure 1.

To fit the line emission, we adopted the slab-modeling Python package `iris` (Munoz-Romero et al. 2023) assuming the gas is in local LTE, with line data from the HITRAN database (Gordon et al. 2022). The line width was estimated with thermal broadening based on the temperature of the gas. In `iris`, the fitting is performed with the Bayesian nested sampling Python package `dynesty` (Speagle 2020). We set the stopping criterion by the change in the remaining evidence (marginal likelihood $\mathcal{Z}$) when $\Delta \log \mathcal{Z} \leq 0.001(n_{live} - 1) + 0.01$, where $n_{live} = 10 \times n_{dim}$ with n_{dim} as the number of parameters in the model.

We restricted the fitting within the wavelength range of 14.0–17.0 μm for the emission of CO_2, and adopted uniform priors for emitting area (A) and column density (N), with $\log_{10} A = \mathcal{U}(-3, 3)$ au^2 and $\log_{10} N = \mathcal{U}(12, 22)$ cm^{-2}. The prior for the gas temperature ($T_{\rm gas}$) was set to be uniform initially, and later set as a normal distribution centered around 500 K with a standard deviation of around 200 K to speed up the search. We included $^{13}CO_2$ with CO_2 in our fitting, and assumed the emissions were from the same region ($T_{\rm gas}$ and A are the same) and the $^{12}C/^{13}C$ ratio was the same as ISM value ($N_{CO_2} = 68 \times N_{^{13}CO_2}$, e.g., Milam et al. 2005). The posterior distributions for the CO2 fitting is shown in Figure C5. The 15.4 μm $^{13}CO_2$ line is

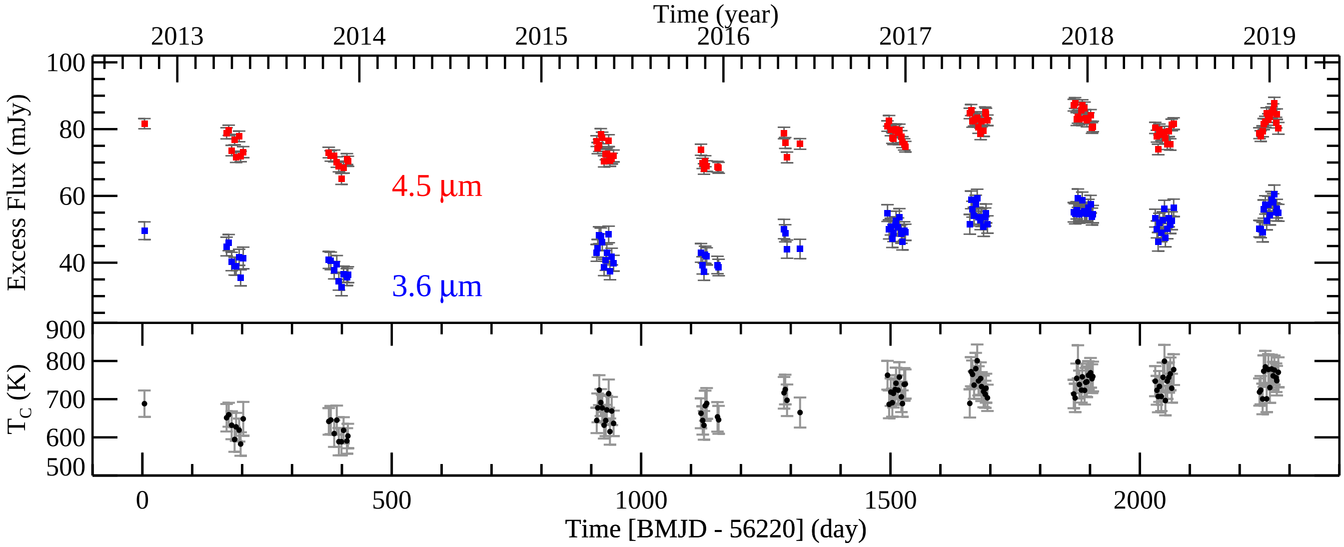

Figure B3. The IR variability around HD 23514 as monitored by warm Spitzer in ∼3-day cadence when available. The upper panel shows the excess fluxes obtained by the two shortest IRAC bands while the bottom depicts the color temperatures derived by the flux ratio. The system exhibits stochastic, weekly variability without obvious periodicity. There exists a weak, positive trend between the excess flux and color temperature.

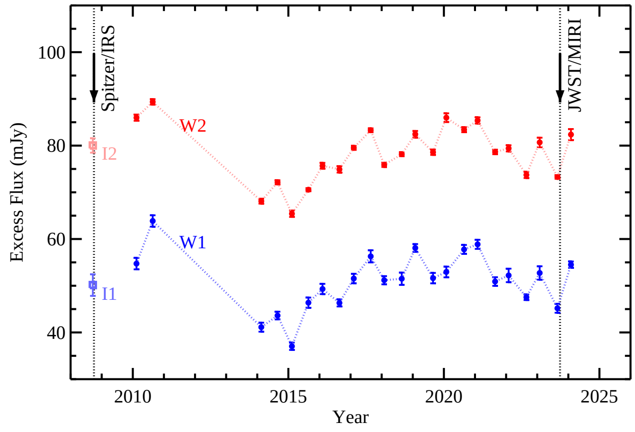

Figure B4. Similar to Figure B3 but with WISE W1 and W2 data along with the Spitzer/IRAC I1 and I2 photometry taken in 2008, showing yearly IR variability. The lowest 3–5 μm flux appeared to be in 2015. The two epochs of mid-IR spectra obtained by Spitzer and JWST were also indicated.

the only (i.e., strongest) isotopologue line present in the data. Excluding it produces a slightly poor fit at 15.4 μm as shown in Figure 2. The best fit CO_2 model parameters were summarized in Table C1 by assuming two different turbulence velocities: 0 km s^{-1} as the nominal and 2 km s^{-1} as the upper limit value. The two cases make very little difference in the resulting fits visually, illustrating the associated uncertainties in the MCMC fits might be underestimated, and reflecting the limitations of using the simple LTE slab model.

Although there are hints of other molecules (CO, H_2O and NH_3) present in the continuum subtracted spectra (Figure C7), we did not attempt to determine their precise parameters using the slab models due to high noise and weak lines. Instead, we assumed they share similar model parameters as CO_2, and adjust N (and A, $T_{\rm gas}$ if necessary) to achieve reasonable fits visually. The mid-infrared emission from molecules is due to ro-vibrational or vibrational transitions and is sensitive to their tem-

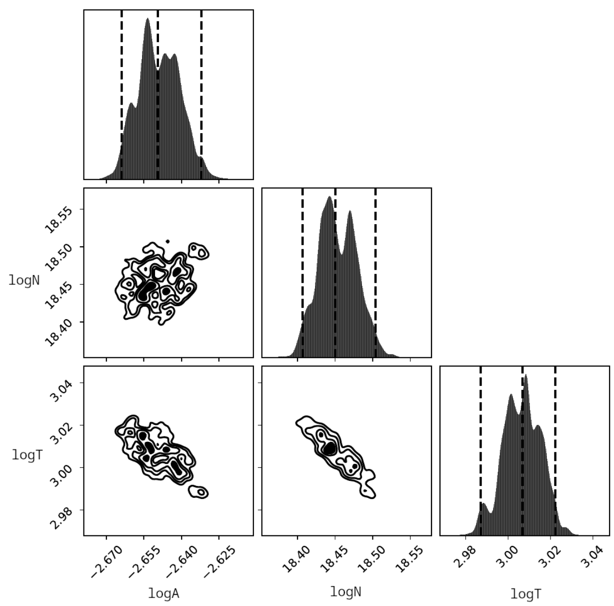

Figure C5. The posterior distributions for the CO_2 fitting using the three parameters: emitting area (log A in units of au^2), column density (log N in units of cm^{-2}), and gas temperatures (log T in units of K).

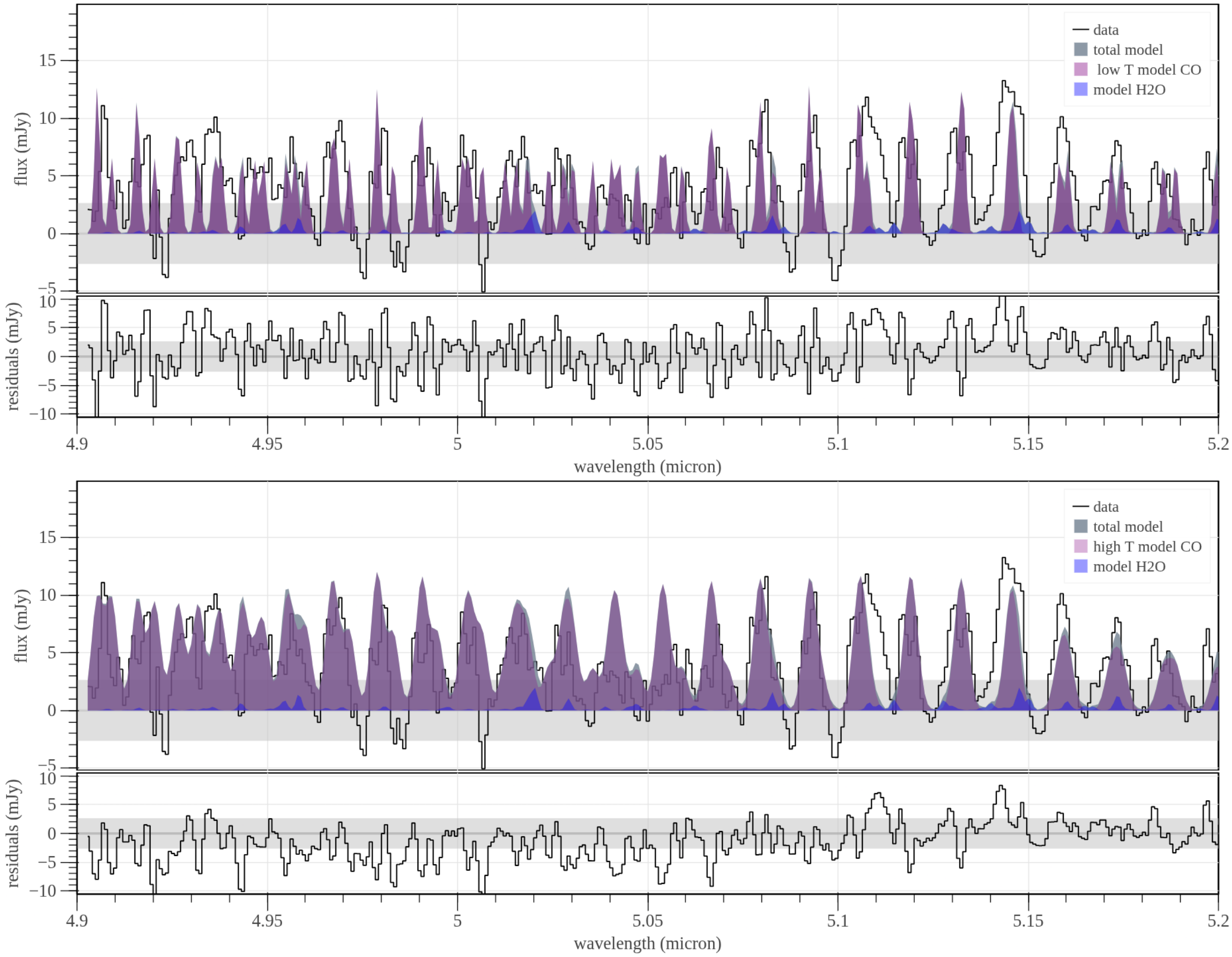

Figure C6. The continuum-subtracted spectrum of HD 23514 centered at the CO gas (upper for the low $T_{\rm gas}$ and lower for the high $T_{\rm gas}$ models; details see Appendix C). The shaded color regions show the slab model predictions of CO (purple) and others (same as Figure 2). For all the comparison plots between the data and model, the flux panels are shown starting from −2 rms to 1.5 times of the peak flux in the displayed segment and the residual panels are all shown in a range of ±4 rms.

Table C1. Best fits CO_2 slab model parameters

parameter	$v_{\rm turb}$=0 km s^{-1}	$v_{\rm turb}$=2 km s^{-1}
$\log_{10} A$ (au^2)	-2.07 ± 0.02	-2.65 ± 0.02
$\log_{10} N$ (cm^{-2})	18.14 ± 0.06	18.45 ± 0.06
$\log_{10} T_{\rm gas}$ (K)	2.95 ± 0.02	3.01 ± 0.02

Note—The uncertainties given in the table are derived from MCMC, which are likely to be underestimated.

peratures, i.e., the lines get significantly weaker as the temperature gets cooler. It is then meaningless to explore lower temperatures (or other parameters) without high S/N data. Keeping the same temperature for both H_2O and NH_3, the column density N needs to be reduced by a factor of ∼2.2 and 1.4, respectively, in order to produce similar flux levels of the lines between 6.5 and 9.5 μm. The low abundance in both H_2O and NH_3 is consistent with their very short photodissociation lifetimes (Figure 5), by $\gtrsim$2–3 order of magnitudes compared to that of CO_2, without shielding. The model parameters for CO, which has the longest photodissociation lifetimes near HD 23514, are very uncertain due to the limited wavelength coverage from MIRI/MRS. The slab model has great difficulty to reproduce the observed line width if CO has a similar $T_{\rm gas}$ as CO_2 (termed low T case in the top panel of Figure C6). Alternatively, the broad width of CO lines can roughly be reproduced by an extra broadening of 200 km s^{-1} and increasing $T_{\rm gas}$ to ∼3000 K (termed high T case in the middle panel of

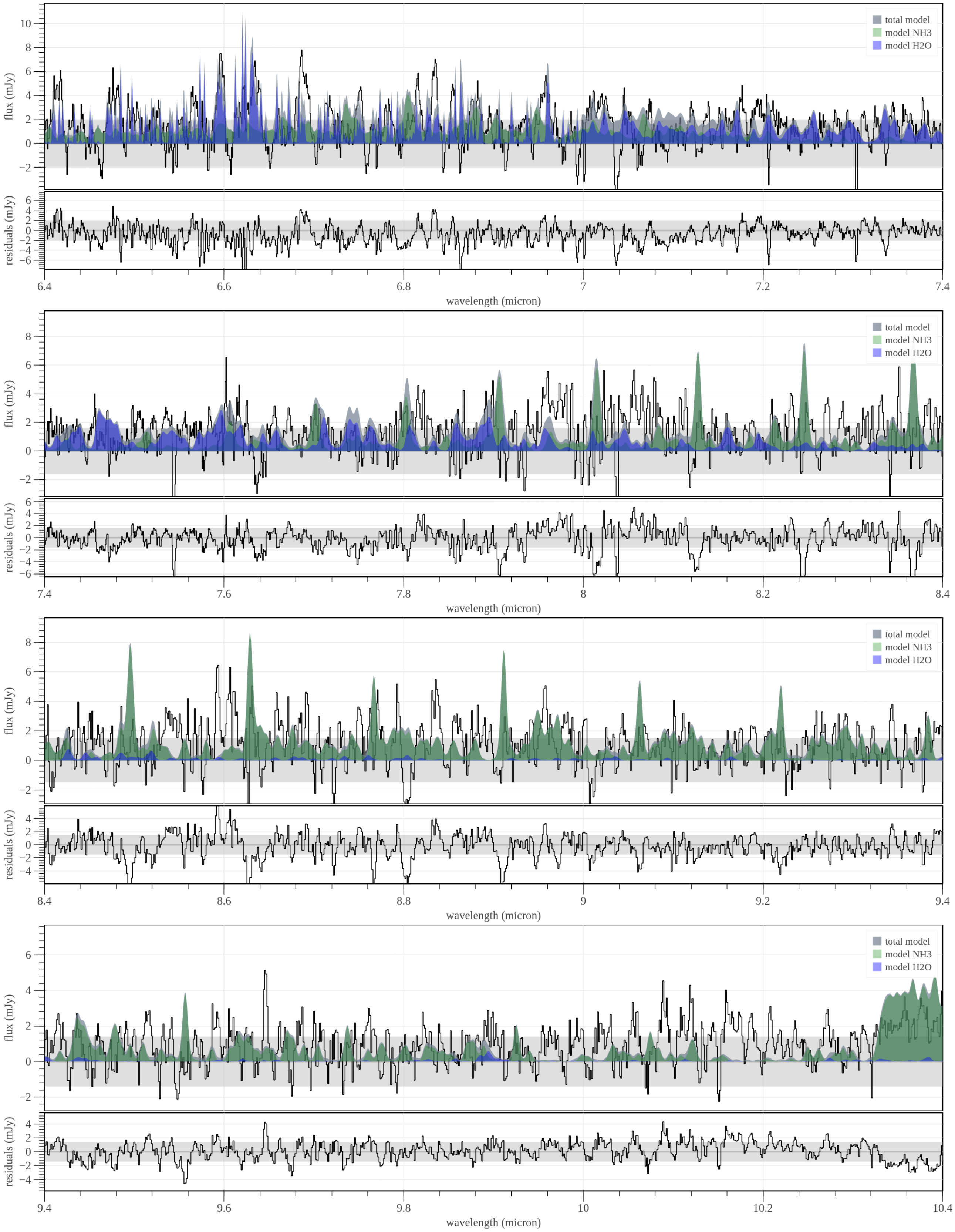

Figure C7. Same as Figure C6 for different spectral segments with different molecules using the same plotting rule.

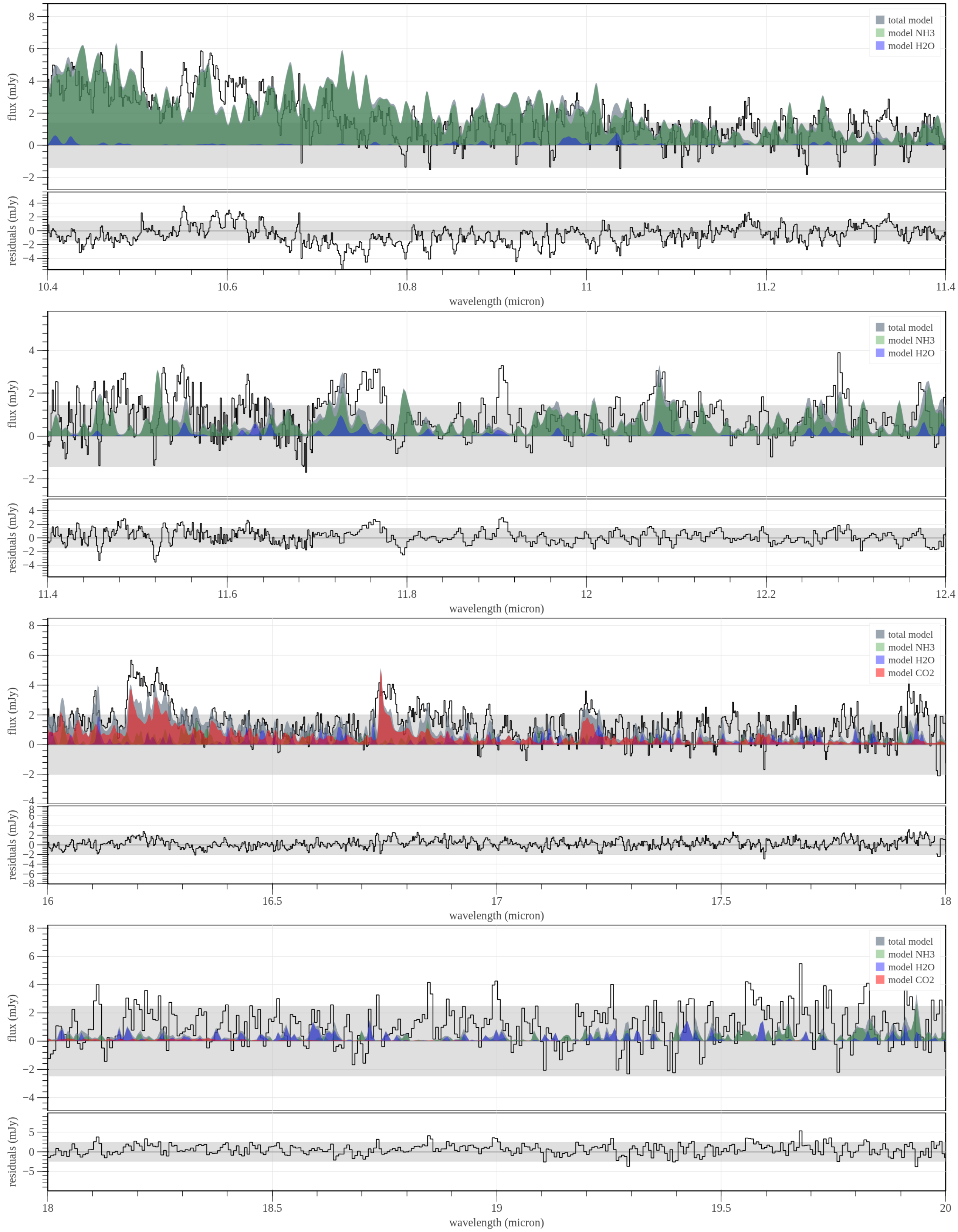

Figure C7. Continue Figure C7

Figure C6). Such a high temperature can be reached at a stellocentric distance of 0.015 au around HD 23514 where its Keplerian velocity (v_K) is ∼277 $\mathrm{km\,s^{-1}}$. This seems to suggest the additional broadening might be related to the Keplerian motion of the CO gas. If the gas is indeed in a disk form, resolving the double-peak profiles in the CO emission could help to constrain the inclination of the system, which should be explored in future better data. For the low $T_{\rm gas}$ CO model, the associated log$N$ and log$A$ are 20.5 $\mathrm{cm^{-2}}$ and -2.0 $\mathrm{au^2}$, but 17.5 $\mathrm{cm^{-2}}$ and -2.5 $\mathrm{au^2}$ for the high $T_{\rm gas}$ model, illustrating the sensitivity to the gas temperature. We note that the CO lines are optically thick in both cases, and that the slab model we used does include the optical depth effects, i.e., the derived N and A are reliable for the assumed temperature.

We can also estimate the minimum gas mass by assuming the emission is optically thin. Taking the slab model parameters at $v_{\rm turb}$ = 0 km $\mathrm{s^{-1}}$, the total gas mass for CO_2, H_2O, and NH_3 is: 3.21×10^{-8}, 6.05×10^{-9} and 5.04×10^{-9} $M_\oplus$, respectively. Note that the mass for H_2O and NH_3 should be considered as upper limits given the tentative detection. The total mass for CO is 5.54×10^{-6} $M_\oplus$ for the low $T_{\rm gas}$ case, but 1.75×10^{-9} $M_\oplus$ for the low $T_{\rm gas}$ case. The total gas mass ranges from 4.5 $\times10^{-8}$ to 5.6×10^{-6} $M_\oplus$ (spreading two orders of mag, depending on the CO mass). Using the Equ. (14) from Birnstiel et al. (2010), we can estimate the Stokes number between the gas and small (0.5 μm) dust by spreading the masses within 0.3 au for simplicity. The Stokes number between the gas and small dust is 0.44 (for the low $T_{\rm gas}$ CO model) or 55 (for the high $T_{\rm gas}$ CO model) assuming a grain density of 3 $\mathrm{g\,cm^{-3}}$). In the former case, the small dust and gas are coupled and the presence of gas would have an impact on dust dynamics, affecting the inward or outward draft rate depending on the gas surface density. In the later case, the tiny amount of gas has no strong effects on dust, i.e., radiation blowout operates on orbital timescales (less than a year in sub-au).

C.2. *Upper Limits on Molecular Hydrogen Gas*

No H_2 lines are detected in the continuum-subtracted spectrum of HD 23514. We used the local rms estimated around ±50 spectral resolution elements around the potential lines to estimate the 3-σ upper limits on the integrated line flux assuming the lines are optically thin and unresolved. Fixing the gas temperature at $T_{\rm gas}$ =9 00 K, we used all the upper limit line fluxes from H_2(S1) to H_2(S8) to estimate the gas mass and found that H_2(S3) line at 9.664 μm (integrated line flux of 3.27×10^{-23} $\mathrm{W\,cm^{-2}}$) gives the best 3-σ upper limit mass, $2.25\times10^{-3} M_\oplus$. The best estimated CO mass is $5.54\times10^{-6} M_\oplus$ (taking from the low $T_{\rm gas}$ = 900 K case), implying the CO-to-H_2 mass ratio is $> 2.5\times10^{-3}$ which is slightly larger than the typical ISM value (an abundance of 10^{-4} translates to a mass ratio of 1.4×10^{-3}. Although the CO-to-H_2 mass ratio cannot unambiguously prove the gas is secondary, the old age of the system and the lack of HI and [Ne II] emission favor non-primordial.

C.3. *Photodissociation Rate and Molecular Shielding Efficiency*

We derived the photodissociation lifetimes for CO, CO_2, H_2O, and NH_3 molecules as a function of stellocentric distance assuming that these molecules are exposed to ultraviolet (UV) photons from both the interstellar radiation field (ISRF) and the star without shielding. The Kurucz model described in Appendix A.1 and the standard ISRF (Draine 1978; van Dishoeck & Black 1982) were adopted, and the relevant photodissociation cross sections were taken from the online database of the Leiden Observatory[14] (Visser et al. 2009; Heays et al. 2017). The result was shown in Figure 5. For all molecules, the UV radiation from the star dominates the photodissociation processes within 10 au. We note that HD 23514 is located in the outer skirt of the Pleiades cluster (far away from the central B-type stars), where the ISRF may be different from that of typical ISM, it does not significantly affect the results within 10 au unless it is very different from the assumed one.

For CO, CO_2, H_2O, and NH_3, UV photons with wavelengths shorter than ∼109, ∼115, ∼180, and ∼207 nm, respectively, are involved in the photodissociation of the molecules. Unfortunately, there are no UV observations available for HD 23514 that would assess the reliability of the adopted Kurucz model at these wavelengths. Since it is a relatively young F5 type star, it is suspected that it may show magnetic activity and thus probably exhibits excess emission in the UV regime. In the case of our Sun, the Kurucz model underestimates the observed emission increasingly towards the shortest wavelengths[15]. Therefore, our photodissociation lifetimes derived for HD 23514 should be considered as upper limits.

UV shielding could occur by the molecule itself (self-shielding), by other molecules and atoms, and by the presence of dust. We investigated the shielding factor (efficiency) for CO_2 by various gases as a function of the column density of the given gases as shown in Figure C8. Two different radiation fields (ISRF and

---

[14] https://home.strw.leidenuniv.nl/~ewine/photo/data/photo/

[15] see the measured spectrum from https://home.strw.leidenuniv.nl/~ewine/photo/data/photo_data/radiation_fields/solar.dat

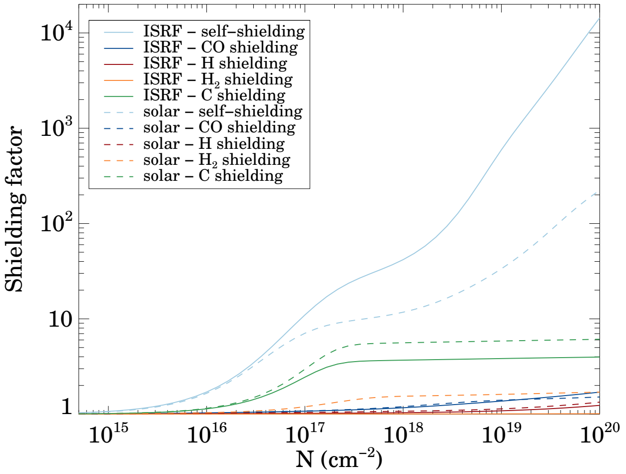

Figure C8. CO_2 shielding efficiency (in terms of factors to prolong the photodissociation lifetime) from different molecules (colored) against photodissociation as a function of column density. Solid lines used the ISRF as the radiation field while the dashed ones from the solar radiation.

solar) were used along with the molecular properties from the Leiden Observatory database (https://home.strw.leidenuniv.nl/~ewine/photo/, Heays et al. 2017). Shielding from CO_2 itself is really efficient once the column density reaching $\sim 10^{18} cm^{-2}$ and can increase its photodissociation lifetime more than tenfold. The dust component of typical debris disks is so dilute that it cannot contribute significantly to the shielding of the molecules. However, in the case of HD 23514, it is conceivable that some parts of the dust disk could be optically thick, which could slightly increase the photodissociation lifetime of the molecules. Nevertheless, the photodissociation lifetime of CO_2 with self-shielding is still very short, on the order of a few days at 0.05 au. Assuming the gas remains stable over 15 years between the Spitzer and JWST observation, the shielding from tiny dust needs to be thousandfold more effective than molecular gas shielding.

C.4. *The Nature of the 15 μm bump in the Spitzer/IRS Spectrum*

We investigated whether the 15 μm bump in the Spitzer spectrum as shown in Figure 3 could be due to data reduction artifacts by examining the CASSIS IRS spectra of a handful debris systems (e.g., HD 172555, HD 15407 and HD 69830 and others), which are brighter or at a similar brightness as HD 23514 and observed in the same observing mode, using the CASSIS products. We found no similar bump near 15 μm, suggesting that the 15 μm bump is likely astrophysical in nature.

D. ESTIMATING THE DUST LOCATION, BLOWOUT SIZES AND VARIOUS TIMESCALES

D.1. *SED Models*

The purpose of the SED modeling is to estimate the disk extent and to illustrate that the bulk of the silica dust is co-located with the hot molecular gas (from the temperature argument). The derived parameters are then used to estimate various timescales that are relevant in HD 23514.

Given the number of assumed parameters, the SED models are extremely degenerate and sensitive to the disk density distribution, and only serve as a zero-order estimate without other constraints like resolved disk images. We stress that the SED modeling results are only applicable to the part of the disk where its bulk emission is fully captured by the SED measurements. The assumptions for our SED models are: (1) the star is the only heating source and in an optically thin environment, (2) there is one single, flat (constant surface density), continuous disk with a radial range of inner ($r_{\rm in}$) and outer ($r_{\rm out}$) radii from the star, and (3) the dust grains are all in one uniform size distribution with a size power-law index of -3.5 and a maximum size of 1000 μm. We explored several minimum grain sizes and found that a minimum size of 0.1–0.5 μm silica- and silicate-like grains are needed in order to produce the prominent 10/20 μm features, even though the typical radiation blowout size is $\sim$1 μm given the stellar mass and luminosity (1.3 $M_\odot$ and $\sim$3 $L_\odot$). The dynamical stability of these small grains is subject to their exact optical properties in response to the stellar radiation, which is not explored/considered here. We consider that the impact of other parameters such as the maximum grain size ($a_{\rm max}$) and surface density power-law is minimal in a way that (1) $a_{\rm max}$ affects the total dust mass in a $\sqrt{a_{\rm max}}$ fashion under the assumed size distribution, and (2) a steeper surface density distribution would extend $r_{\rm out}$ so enough colder material can account for the total emission.

A large uncertainty in our SED model resides in the grain composition. The dust temperatures depend sensitively on the grain absorption efficiency at the wavelengths where the star emits most its energy (i.e., UV and optical for HD 23514). Sub-μm grains are generally hotter than their larger counterparts and the exact temperatures can be vastly different between different types of composition as shown in the left panel of Figure C9. Because the carbonaceous and silica grains are less absorptive than the typical silicates in the UV and optical,

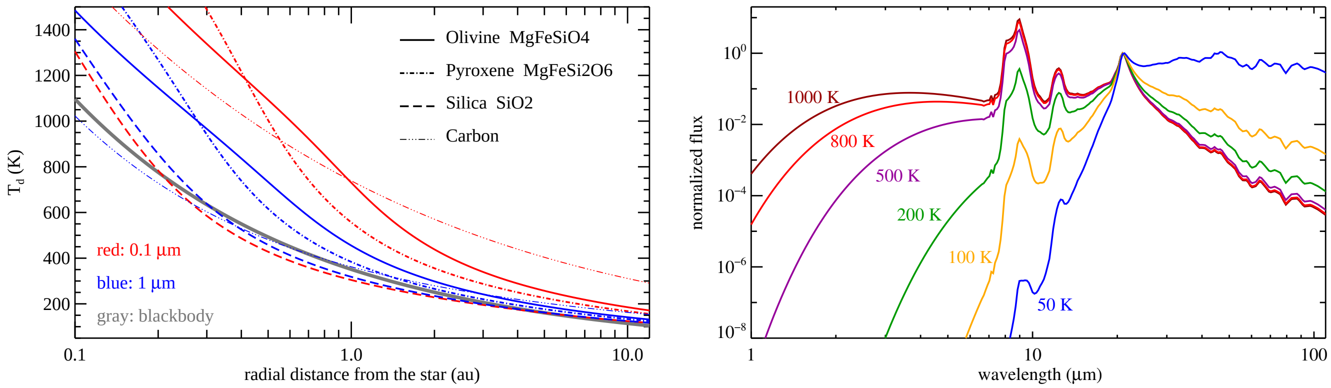

Figure C9. The left panel shows the estimated thermal equilibrium dust temperature as a function or stellocentric distance from HD 23514 under the optically thin condition. Line styles depict different composition with the red for 0.1 μm and the blue for 1 μm grains. The thick gray line represents the temperature for blackbody emitters. The right panel shows the expected SED for 0.1 μm silica grains at different (colored) temperatures normalized at the 20 μm peak, illustrating that the contrast/ratio between the 9 μm and 20 μm is sensitive to the dust temperature.

they generally have lower temperatures than that of silicates at the same stellocentric distance from the star.

Determining detailed dust mineralogy to infer the exact dust composition is beyond the scope of this short paper. We only explored limited dust compositions that are commonly found in thermally processed dust in circumstellar environments. For the dust emission calculation, we adopted the grain properties computed by `optool` (Dominik et al. 2021) using the Distribution of Hollow Spheres (DHS, Min et al. 2005) approach with an irregularity factor $f_{\rm max}$ of 0.8. We found that the system's SED can be well represented by three types of dust: silica (density ρ = 2.65 g cm^{-3}, Henning & Mutschke 1997), pyroxene (ρ = 3.2 g cm^{-3}, Dorschner et al. 1995) and amorphous carbon (ρ = 1.85 g cm^{-3}, Zubko et al. 1996) where the first two give rise to the prominent dust features in the mid-IR while the amorphous carbon and a small fraction of Mg-rich pyroxene grains contribute the underlining featureless dust continuum as shown in Figure 4. A single component disk with $r_{\rm in} = 0.1$ au and $r_{\rm out}$ ~2–3 au gives a good fit to the measured SED except that the silica grains need to be restricted within 0.1–0.2 au to account for enough flux in the 3–5 μm range without changing the contrast/ratio between the 10 and 20 μm features (the right panel of Figure C9). In other words, having silica grains beyond 1 au would shift the near-IR flux toward the far-IR because of its low thermal temperature outside 1 au, resulting in poor fits between 3 and 5 μm. We note that the model produces a much narrower 10 μm feature than the observed one, likely due to the mismatch in the various silica polymorphs (Koike et al. 2013).

Based on the SED model, the system's infrared fractional luminosity (f_d) is $\sim 1.76\times10^{-2}$ with ~70% coming from the featureless dust continuum. The total dust mass is $\sim 10^{24}$ g ($1.67\times10^{-4} M_\oplus$) and the feature-producing grains account for ~5% of the mass. Because the SED models prefer a confined (sub-au) region for the silica grains, the total silica dust mass (integrated to 1 mm in size) is on the order of 1% ($\sim 10^{22}$ g) of the total dust mass. In summary, the bulk of the dust in HD 23514 is within 3 au and the silica dust is mostly located inside a sub-au region, similar to the location of the hot molecular gas found in Appendix C.1. HD 23514 was not detected by the ALMA 1.3 mm shallow survey for the Pleiades (Sullivan et al. 2022), suggesting lack of cold ($\lesssim$40 K) dust, although the ALMA data could not exclude a less dusty planetesimal belt like our current Kuiper belt. In conclusion, the HD 23514 system does not possess a massive (tens of au) Kuiper-belt-like analog that are found in ~20% of solar-like stars (Sierchio et al. 2014; Matrà et al. 2025).

D.2. *Radiation Pressure Blowout Sizes around HD 23514*

In gas-free debris disks, stellar radiation pressure is one of the most important forces acting on grains that counters with the star's gravity and dictates the dust dynamics, which can be characterized by the β parameter defined as the ratio of radiation pressure to gravitational forces, i.e.,

$$\beta = \frac{3\langle Q_{\rm pr}\rangle L_*}{16\pi G c M_* a \rho} \tag{D1}$$

where L_* and M_* are luminosity and mass of the star, a is grain size, ρ is grain density, and $\langle Q_{\rm pr}\rangle$ is the radiation-pressure efficiency averaged over stellar spectrum (Burns et al. 1979). The last three parameters have strong dependency on the exact grain properties (composition, size, density and porosity, as detailed in Arnold et al. 2019). Grains with β > 0.5 get pushed

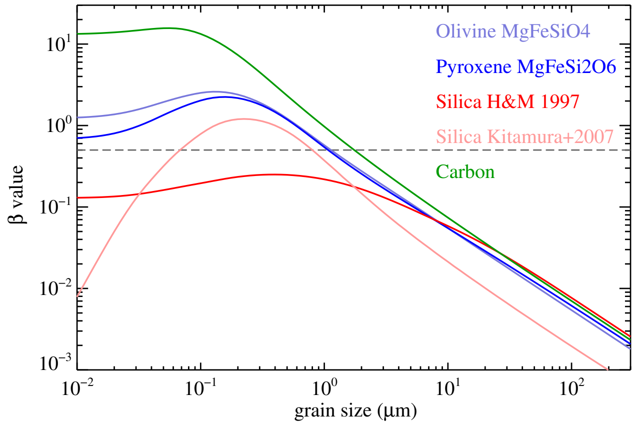

Figure D10. Computed β values, the ratio between radiation pressure and gravitational forces, for different sizes and compositions of ideal dust grains around HD 23514. The horizontal dashed line marks $\beta = 0.5$ where the blowout size is defined and grains above the line are subject to radiation pressure blowout (details see Appendix D.2).

into hyperbolic orbits and leave the system, while grains with $\beta < 0.5$ are on elliptical orbits and spiral inward due to Poynting-Robertson (P-R) drag. The radiation pressure blowout size is defined as $\beta = 0.5$, and the exact size depends on the type of star, and most importantly, the grain properties as illustrated in Figure D10. The *beta* values are calculated using the stellar Kurucz model described in Appendix A.1, the grain compositions adopted in Appendix D.1 with two additions (olivine: $\rho = 3.71$ from Dorschner et al. 1995, and silica: $\rho = 2.65$ from Kitamura et al. 2007), and assuming compact (i.e., ideal with zero porosity) grain shape. For nominal silicate and carbonaceous compositions, grains small than the blowout size ($\sim$1 μm for HD 23514) are ejected and on a terminal velocity of $\sqrt{2(\beta - \frac{1}{2})}v_K$ (Su et al. 2005). While for silica composition, some (such as the one with the optical constant from Henning & Mutschke 1997) could have $\beta < 0.5$ for all sizes, and some (from Kitamura et al. 2007) would have the β >0.5 grains within two blowout sizes. This also illustrates the blowout size is not a strict number, highly depending on the exact composition. We stress the importance of grain optical properties in the UV and optical wavelengths where the star emits most of its energy in estimating the grain's β values.

D.3. *Relevant Timescales*

For a dust-dominated debris disk, the dominant grain loss mechanisms are collisional grinding and P-R/stellar wind drags. Once the grains generated by collisional cascades are smaller than the radiation blowout size ($\sim$1 μm in HD 23514 when the ratio between the radiation pressure force and gravity, defined as β, equal to 0.5), they are ejected from the system by radiation pressure under normal conditions. The blowout timescale is on the order of the orbital period, which is relatively fast (1.3 week at 0.1 au, 0.8 yr at 1 au, and 4.5 yr at 3 au around an 1.3 $M_\odot$ star), although the the presence of overabundant sub-μm grains suggests that such rapid removal is not taking place in this system, likely due to the presence of gas. HD 23514's chromospheric activity index (Fang et al. 2018) indicates that its stellar wind should not be exceptionally strong, suggesting the drag force is dominated by the P-R drag with timescales $\tau_{PR} = cr^2/(4GM_*\beta) \sim 800$ yr $(r/\mathrm{au})^2(M_\odot/M_*)(0.5/\beta)$ where c is the speed of light, G is the gravitational constant, and M_* is the stellar mass. Within 1 au, the P-R timescale is a few 100s yr in HD 23514.

Collisional grinding operates in a cascade fashion among different sizes of particles with a loss time that depends on the properties of the particle swarm (belt location and width, total mass and the size of the particle) and stellar mass. Continuous grindings supply enough new grains against the loss from radiation blowout and P-R drag, therefore sustaining the dust level over the collisional timescales (τ_c). The collisional timescale can be estimated as formulated by Equ.(13) in Wyatt et al. 2007 where the largest unknown properties are the total disk mass (M_{tot}), the maximum size (D_c) of the planetesimals, and belt location (r).

Based on the SED modeling described above, we can set r $\sim$3 au with a width $dr = 0.1\,r$ for simplicity. If we take the SED derived dust mass (up to 1 mm) at the face value, τ_c is $\sim$500 yr for D_c of 1 mm. However, if we extrapolate the dust mass to 1 km size planetesimals (i.e., 0.167 $M_\oplus$ as the disk mass), τ_c $\sim 5\times10^5$ yr in this case. The collisional timescale is inversely proportional to the total disk mass if extrapolated to larger size of planetesimal (by a factor of $\sqrt{a_{\mathrm{max}}}$), and is directly related to the size of colliding bodies. If the disk in HD 23514 formed by a past giant impact at 3 au, it would remain infrared bright for $\gtrsim 10^{3-4}$ yr, consistent with the previous studies (Jackson & Wyatt 2012).

An alternative way to support the giant impact hypothesis for HD 23514 is to examine the mass loss rate and back track M_{tot}. From the SED model, we estimate the dust mass for the small grains, the ones that give rise to the solid-state feature, is $\sim 5 \times 10^{22}$ g. These $\lesssim$1 μm grains are expected to be ejected from the system on the blowout timescale, which is $\lesssim$1 yr in HD 23514. Sustaining this high mass loss rate through collisional cascades would requires a total planetesimal mass of $\sim$1260 $M_\oplus$ over the age of the star (150 Myr) (without counting the loss from P-R drag). This would require that HD 23514 has a 35 times more mass than the minimum mass solar nebula (MMSN) at birth (assuming 100:1 gas to dust mass ratio). It is then unlikely such a high rate has been sustained over the age of the system, i.e., the high mass loss rate is transient, consistent with the giant impact hypothesis.

Facilities: JWST (MIRI), Spitzer, WISE

Software: `astropy` (Astropy Collaboration et al. 2022), `scipy` (Virtanen et al. 2020)

ACKNOWLEDGMENTS

Work on this paper was supported by grants 80NSSC18K0555 from NASA Goddard Space Flight Center to the University of Arizona, and by 80NSSC20K1002 under the NASA ADAP program. AM is supported by the Hungarian National Research, Development and Innovation Office Élvonal grant KKP-143986. AK acknowledges the support by the NKFIH NKKP grant ADVANCED 149943 and the NKFIH excellence grant TKP2021-NKTA-64. Project no.149943 has been implemented with the support provided by the Ministry of Culture and Innovation of Hungary from the National Research, Development and Innovation Fund, financed under the NKKP ADVANCED funding scheme. PA is partially supported by the Hungarian NKFIH grant K-147380. LM and ZR acknowledges funding by the European Union through the E-BEANS ERC project (grant number 100117693). Views and opinions expressed are however those of the author(s) only and do not necessarily reflect those of the European Union or the European Research Council Executive Agency. Neither the European Union nor the granting authority can be held responsible for them.

This research has made use of the NASA/IPAC Infrared Science Archive, which is funded by the National Aeronautics and Space Administration and operated by the California Institute of Technology.

The data presented in this article were obtained from the Mikulski Archive for Space Telescopes (MAST) at the Space Telescope Science Institute. These observations are associated with JWST program 1206. The standard pipeline-processed products can be accessed via doi:10.17909/qwmm-1c59.

REFERENCES

Abe, Y., & Matsui, T. 1985, Lunar and Planetary Science Conference Proceedings, 90, C545

Arnold, J. A., Weinberger, A. J., Videen, G., & Zubko, E. S. 2019, AJ, 157, 157, doi: 10.3847/1538-3881/ab095e

Artymowicz, P. 1988, ApJL, 335, L79, doi: 10.1086/185344

Astropy Collaboration, Price-Whelan, A. M., Lim, P. L., et al. 2022, ApJ, 935, 167, doi: 10.3847/1538-4357/ac7c74

Bedding, T. R., Murphy, S. J., Crawford, C., et al. 2023, ApJL, 946, L10, doi: 10.3847/2041-8213/acc17a

Beust, H., Lagrange, A. M., Plazy, F., & Mouillet, D. 1996, A&A, 310, 181

Birnstiel, T., Dullemond, C. P., & Brauer, F. 2010, A&A, 513, A79, doi: 10.1051/0004-6361/200913731

Bonsor, A., Wyatt, M. C., Marino, S., et al. 2023, MNRAS, 526, 3115, doi: 10.1093/mnras/stad2912

Bosman, A. D., Bruderer, S., & van Dishoeck, E. F. 2017, A&A, 601, A36, doi: 10.1051/0004-6361/201629946

Burns, J. A., Lamy, P. L., & Soter, S. 1979, Icarus, 40, 1, doi: 10.1016/0019-1035(79)90050-2

Bushouse, H., Eisenhamer, J., Dencheva, N., et al. 2024, JWST Calibration Pipeline, 1.15.1, Zenodo, doi: 10.5281/zenodo.12692459

Canup, R. M. 2004, Icarus, 168, 433, doi: 10.1016/j.icarus.2003.09.028

Cutri, R. M., Wright, E. L., Conrow, T., et al. 2012, Explanatory Supplement to the WISE All-Sky Data Release Products, Explanatory Supplement to the WISE All-Sky Data Release Products

de Wit, W. J., Grinin, V. P., Potravnov, I. S., et al. 2013, A&A, 553, L1, doi: 10.1051/0004-6361/201220715

Dent, W. R. F., Wyatt, M. C., Roberge, A., et al. 2014, Science, 343, 1490, doi: 10.1126/science.1248726

Dominik, C., Min, M., & Tazaki, R. 2021, OpTool: Command-line driven tool for creating complex dust opacities, Astrophysics Source Code Library, record ascl:2104.010. http://ascl.net/2104.010

Dorschner, J., Begemann, B., Henning, T., Jaeger, C., & Mutschke, H. 1995, A&A, 300, 503

Draine, B. T. 1978, ApJS, 36, 595, doi: 10.1086/190513

Fang, X.-S., Zhao, G., Zhao, J.-K., & Bharat Kumar, Y. 2018, MNRAS, 476, 908, doi: 10.1093/mnras/sty212

Fu, X., Bragaglia, A., Liu, C., et al. 2022, A&A, 668, A4, doi: 10.1051/0004-6361/202243590

Fujiwara, H., Onaka, T., Yamashita, T., et al. 2012, ApJL, 749, L29, doi: 10.1088/2041-8205/749/2/L29

Furukawa, Y., Nakazawa, H., Sekine, T., & Kakegawa, T. 2007, Earth and Planetary Science Letters, 258, 543, doi: 10.1016/j.epsl.2007.04.014

Gaia Collaboration, Brown, A. G. A., Vallenari, A., et al. 2021, A&A, 649, A1, doi: 10.1051/0004-6361/202039657

Gaidos, E., Jacobs, T., LaCourse, D., et al. 2019, MNRAS, 488, 4465, doi: 10.1093/mnras/stz1942

Gordon, I. E., Rothman, L. S., Hargreaves, R. J., et al. 2022, JQSRT, 277, 107949, doi: 10.1016/j.jqsrt.2021.107949

Harker, D. E., Wooden, D. H., Kelley, M. S. P., & Woodward, C. E. 2023, PSJ, 4, 242, doi: 10.3847/PSJ/ad0382

Heays, A. N., Bosman, A. D., & van Dishoeck, E. F. 2017, A&A, 602, A105, doi: 10.1051/0004-6361/201628742

Henning, T. 2010, Astromineralogy, Vol. 815, doi: 10.1007/978-3-642-13259-9

Henning, T., & Mutschke, H. 1997, A&A, 327, 743

Ilin, E., Schmidt, S. J., Davenport, J. R. A., & Strassmeier, K. G. 2019, A&A, 622, A133, doi: 10.1051/0004-6361/201834400

Ishihara, D., Onaka, T., Kataza, H., et al. 2010, A&A, 514, A1, doi: 10.1051/0004-6361/200913811

Jackson, A. P., & Wyatt, M. C. 2012, MNRAS, 425, 657, doi: 10.1111/j.1365-2966.2012.21546.x

Johnson, B. C., & Melosh, H. J. 2012, Icarus, 217, 416, doi: 10.1016/j.icarus.2011.11.020

Johnson, B. C., Lisse, C. M., Chen, C. H., et al. 2012, ApJ, 761, 45, doi: 10.1088/0004-637X/761/1/45

Juhász, A., Bouwman, J., Henning, T., et al. 2010, ApJ, 721, 431, doi: 10.1088/0004-637X/721/1/431

Kennedy, G. M., & Wyatt, M. C. 2013, MNRAS, 433, 2334, doi: 10.1093/mnras/stt900

Kenyon, S. J., Najita, J. R., & Bromley, B. C. 2016, ApJ, 831, 8, doi: 10.3847/0004-637X/831/1/8

Kitamura, R., Pilon, L., & Jonasz, M. 2007, ApOpt, 46, 8118, doi: 10.1364/AO.46.008118

Koike, C., Noguchi, R., Chihara, H., et al. 2013, ApJ, 778, 60, doi: 10.1088/0004-637X/778/1/60

Lange, M. A., & Ahrens, T. J. 1982, Icarus, 51, 96, doi: 10.1016/0019-1035(82)90031-8

Law, D. R., Argyriou, I., Gordon, K. D., et al. 2025, AJ, 169, 67, doi: 10.3847/1538-3881/ad9685

Lebouteiller, V., Barry, D. J., Spoon, H. W. W., et al. 2011, ApJS, 196, 8, doi: 10.1088/0067-0049/196/1/8

Lebreton, J., van Lieshout, R., Augereau, J. C., et al. 2013, A&A, 555, A146, doi: 10.1051/0004-6361/201321415

Lisse, C. M., Chen, C. H., Wyatt, M. C., et al. 2009, ApJ, 701, 2019, doi: 10.1088/0004-637X/701/2/2019

Lisse, C. M., Meng, H. Y. A., Sitko, M. L., et al. 2020, ApJ, 894, 116, doi: 10.3847/1538-4357/ab7b80

Liu, Y., Pascucci, I., & Henning, T. 2019, A&A, 623, A106, doi: 10.1051/0004-6361/201834418

Lodieu, N., Pérez-Garrido, A., Smart, R. L., & Silvotti, R. 2019, A&A, 628, A66, doi: 10.1051/0004-6361/201935533

Marino, S., Wyatt, M. C., Panić, O., et al. 2017, MNRAS, 465, 2595, doi: 10.1093/mnras/stw2867

Matrà, L., Wyatt, M. C., Wilner, D. J., et al. 2019, AJ, 157, 135, doi: 10.3847/1538-3881/ab06c0

Matrà, L., Marino, S., Wilner, D. J., et al. 2025, A&A, 693, A151, doi: 10.1051/0004-6361/202451397

Melis, C., Olofsson, J., Song, I., et al. 2021, arXiv e-prints, arXiv:2104.06448. https://arxiv.org/abs/2104.06448

Meng, H. Y. A., Rieke, G. H., Su, K. Y. L., et al. 2012, ApJL, 751, L17, doi: 10.1088/2041-8205/751/1/L17

Meng, H. Y. A., Su, K. Y. L., Rieke, G. H., et al. 2014, Science, 345, 1032, doi: 10.1126/science.1255153

Mermilliod, J. C., Mayor, M., & Udry, S. 2009, A&A, 498, 949, doi: 10.1051/0004-6361/200810244

Milam, S. N., Savage, C., Brewster, M. A., Ziurys, L. M., & Wyckoff, S. 2005, ApJ, 634, 1126, doi: 10.1086/497123

Min, M., Hovenier, J. W., & de Koter, A. 2005, A&A, 432, 909, doi: 10.1051/0004-6361:20041920

Moór, A., Curé, M., Kóspál, Á., et al. 2017, ApJ, 849, 123, doi: 10.3847/1538-4357/aa8e4e

Moór, A., Ábrahám, P., Szabó, G., et al. 2021, ApJ, 910, 27, doi: 10.3847/1538-4357/abdc26

Moór, A., Ábrahám, P., Su, K. Y. L., et al. 2024, MNRAS, 528, 4528, doi: 10.1093/mnras/stae155

Morlok, A., Stojic, A., Weber, I., et al. 2016, Icarus, 278, 162, doi: 10.1016/j.icarus.2016.06.013

Moshir, M., Kopman, G., & Conrow, T. A. O. 1992, IRAS Faint Source Survey, Explanatory supplement version 2

Munoz-Romero, C. E., Banzatti, A., & Öberg, K. I. 2023, iris (InfraRed Isothermal Slabs), Zenodo, doi: 10.5281/zenodo.10369000

Naoz, S. 2016, ARA&A, 54, 441, doi: 10.1146/annurev-astro-081915-023315

Pascucci, I., Hollenbach, D., Najita, J., et al. 2007, ApJ, 663, 383, doi: 10.1086/518535

Pearce, T. D., Krivov, A. V., & Booth, M. 2020, MNRAS, 498, 2798, doi: 10.1093/mnras/staa2514

Pontoppidan, K. M., Salyk, C., Banzatti, A., et al. 2024, ApJ, 963, 158, doi: 10.3847/1538-4357/ad20f0

Quintana, E. V., Barclay, T., Borucki, W. J., Rowe, J. F., & Chambers, J. E. 2016, ApJ, 821, 126, doi: 10.3847/0004-637X/821/2/126

Rhee, J. H., Song, I., & Zuckerman, B. 2008, ApJ, 675, 777, doi: 10.1086/524935

Rieke, G. H., Gáspár, A., & Ballering, N. P. 2016, ApJ, 816, 50, doi: 10.3847/0004-637X/816/2/50

Rieke, G. H., Su, K. Y. L., Melis, C., & Gáspár, A. 2021, ApJ, 918, 71, doi: 10.3847/1538-4357/ac0dc4

Rinaldi, G., Della Corte, V., Fulle, M., et al. 2017, MNRAS, 469, S598, doi: 10.1093/mnras/stx1873

Roberge, A., Feldman, P. D., Lagrange, A. M., et al. 2000, ApJ, 538, 904, doi: 10.1086/309157

Rodriguez, D. R., Marois, C., Zuckerman, B., Macintosh, B., & Melis, C. 2012, ApJ, 748, 30, doi: 10.1088/0004-637X/748/1/30

Román-Zúñiga, C. G., Kounkel, M., Hernández, J., et al. 2023, AJ, 165, 51, doi: 10.3847/1538-3881/aca3a4

Samland, M., Henning, T., Garatti, A. C. o., et al. 2025, arXiv e-prints, arXiv:2506.09976, doi: 10.48550/arXiv.2506.09976

Sargent, B., Forrest, W. J., D'Alessio, P., et al. 2006, ApJ, 645, 395, doi: 10.1086/504283

Sargent, B. A., Forrest, W. J., Tayrien, C., et al. 2009, ApJ, 690, 1193, doi: 10.1088/0004-637X/690/2/1193

Schaefer, L., & Fegley, B. 2010, Icarus, 208, 438, doi: 10.1016/j.icarus.2010.01.026

Schneiderman, T., Matrà, L., Jackson, A. P., et al. 2021, Nature, 598, 425, doi: 10.1038/s41586-021-03872-x

Sierchio, J. M., Rieke, G. H., Su, K. Y. L., & Gáspár, A. 2014, ApJ, 785, 33, doi: 10.1088/0004-637X/785/1/33

Speagle, J. S. 2020, MNRAS, 493, 3132, doi: 10.1093/mnras/staa278

Su, K. Y. L., Kennedy, G. M., Schlawin, E., Jackson, A. P., & Rieke, G. H. 2022, ApJ, 927, 135, doi: 10.3847/1538-4357/ac4bbb

Su, K. Y. L., Rieke, G. H., Melis, C., et al. 2020, ApJ, 898, 21, doi: 10.3847/1538-4357/ab9c9b

Su, K. Y. L., Rieke, G. H., Misselt, K. A., et al. 2005, ApJ, 628, 487, doi: 10.1086/430819

Su, K. Y. L., Jackson, A. P., Gáspár, A., et al. 2019, AJ, 157, 202, doi: 10.3847/1538-3881/ab1260

Su, K. Y. L., Kennedy, G. M., Rieke, G. H., et al. 2023, ApJ, 959, 43, doi: 10.3847/1538-4357/ad04d9

Sullivan, D., Wilner, D. J., Matrà, L., et al. 2022, AJ, 164, 100, doi: 10.3847/1538-3881/ac80c5

Takarada, T., Sato, B., Omiya, M., Hori, Y., & Fujii, M. S. 2020, PASJ, 72, 104, doi: 10.1093/pasj/psaa105

Takeuchi, T., & Artymowicz, P. 2001, ApJ, 557, 990, doi: 10.1086/322252

Thebault, P., & Kral, Q. 2019, A&A, 626, A24, doi: 10.1051/0004-6361/201935341

Thompson, M. A., Telus, M., Schaefer, L., et al. 2021, Nature Astronomy, 5, 575, doi: 10.1038/s41550-021-01338-8

Tsantaki, M., Pancino, E., Marrese, P., et al. 2022, A&A, 659, A95, doi: 10.1051/0004-6361/202141702

van Dishoeck, E. F., & Black, J. H. 1982, ApJ, 258, 533, doi: 10.1086/160104

Vican, L., Schneider, A., Bryden, G., et al. 2016, ApJ, 833, 263, doi: 10.3847/1538-4357/833/2/263

Virtanen, P., Gommers, R., Oliphant, T. E., et al. 2020, Nature Methods, 17, 261, doi: 10.1038/s41592-019-0686-2

Visser, R., van Dishoeck, E. F., & Black, J. H. 2009, A&A, 503, 323, doi: 10.1051/0004-6361/200912129

Watson, D. M., Leisenring, J. M., Furlan, E., et al. 2009, ApJS, 180, 84, doi: 10.1088/0067-0049/180/1/84

Watt, L., Leinhardt, Z. M., & Carter, P. J. 2024, MNRAS, 527, 7749, doi: 10.1093/mnras/stad3606

Wright, E. L., Eisenhardt, P. R. M., Mainzer, A. K., et al. 2010, AJ, 140, 1868, doi: 10.1088/0004-6256/140/6/1868

Wyatt, M. C., Smith, R., Greaves, J. S., et al. 2007, ApJ, 658, 569, doi: 10.1086/510999

Young, S. D., & Wyatt, M. C. 2024, MNRAS, 527, 5244, doi: 10.1093/mnras/stad2963

Zubko, V. G., Mennella, V., Colangeli, L., & Bussoletti, E. 1996, MNRAS, 282, 1321

Zuckerman, B. 2015, ApJ, 798, 86, doi: 10.1088/0004-637X/798/2/86